International Journal of Applied Engineering Research ISSN 0973-4562 Volume 12, Number 21 (2017) pp. 10505-10529

An Insight into the Rotational Augmentation on HAWTs by means of CFD Simulations – Part II: Post-Processing and Force Analysis

Mauro S.[1,*], Lanzafame R.[2] and Messina M.[3]

[1,2,3] Department of Industrial Engineering, University of Catania, Viale A. Doria, 6 – 95125 Catania, Italy.

** Corresponding author*

[1]Orcid 0000-0002-5377-7628, [1]Scopus Author ID: 55485143400

[1]Researcher ID: F-3291-2013

Abstract

The interesting results obtained in the first part of this work, led the authors to further study the fluid dynamic behavior of rotating blades. This was done in order to improve the physical comprehension of the rotational augmentation and to provide new ideas and explanations on its onset and development. Three operative conditions were analyzed in-depth: an attached flow condition, at low AoAs; a maximum augmentation condition at medium AoAs; and a fully separated condition at high AoAs. A comparison between 2D airfoil and 3D results was made as well. Post-processing images of streamlines, pressure contours, pressure coefficient trends and helicity contours were thus obtained, demonstrating the presence of a coherent helical structure in the inner blade at medium AoAs. The development of such a structure explained the strong flow acceleration and thus the depressurization of the suction side of the blade. Therefore the helical vortex was found to be mainly responsible for the lift and drag augmentation. Moreover, from an accurate analysis of the forces acting on a fluid element, it was shown that the radial component of the Coriolis forces was the main factor, responsible for the helical structure onset. This Coriolis component acted in an imbalance with the centrifugal force and the spanwise pressure gradient inside the entire separated layer, triggering the 3D flow tangle. The streamwise component of the Coriolis force, instead, was finally found to be of minor importance. Further confirmations derived from the 3D CFD simulations of the rotor fixed wing.

Keywords: HAWT, CFD Transition Modeling, Centrifugal Pumping, Rotational Augmentation

INTRODUCTION

In order to find an explanation for the interesting trend of the aerodynamic coefficients and on the considerations made on it in part I of this work, the authors further analyzed the fluid dynamic behavior of the rotating blade, post-processing the rotor CFD 3D simulations in three specific conditions: an attached flow condition, at low AoAs (≈ 5°); a maximum lift condition, at medium AoAs (≈ 37°); a fully separated condition, at high AoAs (≈ 60°). Furthermore, for each condition, an inner (r/R 34%), a medium (r/R 65%) and an outer (r/R 95%) radial station were considered for extrapolating images, data and parameters. In this way, a wide range of blade conditions was evaluated. In addition, different wind and rotational speed combinations, which led to similar AoAs, were analyzed in order to demonstrate that the velocities did not significantly influence the fluid dynamics, as previously supposed. A comparison with 2D simulations was made as well, thus demonstrating how the flow-field was influenced by rotation. Based on this analysis the authors concluded that the onset of a coherent helical vortex in the inner blade was mostly responsible for the strong depressurization of the suction side. This led to a fluid dynamic behavior comparable to that of a typical inviscid flow. Indeed, the separated layer was found to be almost reattached at medium AoAs (30° - 40°) due to the suction generated by the vortex. In order to better understand the reason for the development of the helical vortex, a force analysis was obtained by using Fluent post-processing data. The radial forces were compared to the radial velocity at many chords and radial positions, finding a truly interesting correlation. The preponderance of the radial component of the Coriolis force, instead of the stream-wise component, was demonstrated to be the most important cause for the triggering of the helical vortex and thus for the rotational augmentation. The complex mechanism that triggered the onset of the helical structure was also due to the vertical shear over the suction side of the blade caused by the tilting of the radial force and velocity between the upper and the lower separated layers. Lastly, the simulation results of the rotor fixed blade demonstrated that the effects of the radial forces and, more specifically, the effects of radial component of the Coriolis force were preponderant compared to the simple spanwise pressure gradient. The comprehension of the complex 3D phenomena, related to the rotating blades, was thus much improved, leading the way for a better modeling of the rotational augmentation inside the simplified 1D codes.

2D – 3D POST-PROCESSING COMPARISONS AND CONSIDERATIONS

Low AoAs analysis: attached and stall delay flow condition

For the low AoAs, two operative conditions were post-processed as reported in Tab. 1. The comparison was made with the relative 2D AoAs and Reynolds number conditions as well.

The combination of V_w = 5 m/s with n = 2,500 r/min (named as condition A) and V_w = 10 m/s with n = 4,500 r/min (named as condition B) led to similar 3D AoA at the examined radial stations. It is virtually impossible to obtain exactly the same values. However, the comparison is quite significant, as demonstrated in the figures hereinafter.

Starting from the inner blade analysis (r/R 34%) in Tab. 1 a substantial equivalence is evident. Despite the rather different rotational speed, the lift and drag coefficients are comparable, considering the slightly higher AoA for condition B. The 3D data, in this case, are compatible with 2D values confirming the fact that the rotational effects are not of the utmost importance at low AoAs. In Fig. 1, only slight differences in flow-field and pressure distributions are detectable.

In Fig. 2 the 3D streamlines, starting from a cylindrical section at r/R 34%, demonstrate the substantial equivalence of the flow-field for both A and B conditions. The images refer to the suction side of the blade. The radial flow component is evidently similar in both cases. Unlike the 2D case, where the separation leads to the generation of a recirculation area [1 - 7], in the 3D case the flow is pushed from the inner to the outer blade, so that the flow cannot be considered actually reattached. This is further evidenced in Fig. 3, where the surface streamlines of wall shear show the net separation between the truly attached flow and the radial flow zone.

In Tab. 1 a Maximum Velocity Ratio (MVR) (1) parameter appears. This parameter was defined by the authors and is simply the ratio between the maximum flow velocity on the suction side of the airfoil in a cylindrical section and the relative velocity in that cylindrical section. This must be at sufficient distance from the rotor (thus resulting in an undisturbed velocity). The reason for the definition of a MVR is explained as follows: it is widely known that the depressurization of the suction side of an airfoil is strictly related to the flow acceleration. Higher velocity means higher depressurization and thus higher aerodynamic forces. By defining a ratio between the maximum velocity and the relative velocity, one can easily highlight the depressurization due to rotation at different operative conditions (radial stations as well) and even further highlight how the rotation influences the forces thanks to an additional acceleration on the suction side compared to a simple 2D condition. The MVR in 2D is simply the ratio between the maximum velocity on the suction side and the relative velocity at the inlet. Furthermore, this normalization allowed for an adequate comparison between flow-fields related to airfoils with different chords and equal Reynolds numbers. For example, in 2D the reference chord was 1m, while in the rotor the chord was only a few centimeters. In order to get similar Reynolds numbers, the flow speed must be much lower in 2D so that a direct comparison of the velocity magnitude was not significant.

$$MVR = \frac{V_{s\,max}}{V_R} \quad (1)$$

Table 1: Extrapolated data for different 2D – 3D conditions for attached flow

CFD 3D						
Wind and rotational speed	**V_w = 5 – n = 2,500 (A)**			**V_w = 10 – n = 4,500 (B)**		
r/R [%]	34	65	95	34	65	95
AoA [deg]	5.3	2.6	3.1	6.6	3.7	3.9
C_l [-]	0.38	0.25	0.17	0.49	0.43	0.27
C_d [-]	0.06	0.045	0.036	0.06	0.037	0.03
MVR	1.3	1.3	1.24	1.35	1.35	1.28
Mean Re	25,000			40,000		
CFD 2D						
AoA [deg]	5	3		6	4	
C_l [-]	0.37	0.22		0.52	0.401	
C_d [-]	0.072	0.059		0.071	0.058	
MVR	1.25	1.29		1.31	1.35	

In (1) $V_{s\,max}$ is the maximum suction velocity and V_R is the relative velocity far from the rotor in a cylindrical section. V_R clearly differs from V_r which, in 3D, is affected by rotor induction. MVR substantially takes into account how much the flow is accelerated on the suction side.

Here, in the 3D case, for condition A, $V_{s\,max}$ = 13.8 m/s and V_R = 10.6 m/s while for condition B, $V_{s\,max}$ = 26.6 m/s and V_R = 19.7 m/s thus corresponding to $MVR_{3D}(A)$ = 1.3 and $MVR_{3D}(B)$ = 1.35. In 2D, instead, for AoA = 5°, Re = 25,000 (condition A), $V_{s\,max}$ =0.47 m/s and V_R = 0.36 m/s while for AoA = 6°, Re = 40,000 (condition B), $V_{s\,max}$ = 0.79 m/s, V_R =0.58 m/s that lead to $MVR_{2D}(A)$ = 1.25 and $MVR_{2D}(B)$ = 1.31. From the 2D – 3D MVR comparison a substantial equivalence of the suction side flow acceleration is evident. This is in agreement with the equivalence of the aerodynamic coefficients. The flow acceleration is around 30% both in 2D and 3D cases confirming that, in this case, the rotational augmentation is not of the utmost importance.

Very similar considerations may be done for r/R 65% and r/95% sections, therefore the results are not presented here. It is interesting to notice, however, that due to the presence of the radial effect, the flow-field is rather similar at all the radial stations. The pressure distribution on the suction side is comparable as well. This further confirm that the rotation, at low AoAs, acts by stabilizing the boundary layer separation thus leading to a fluid dynamic behavior that is typical for the

fully attached flow condition. Furthermore, the influences of the Reynolds number (earlier separation and higher laminar bubbles instability at low Re [1 - 8]) are canceled along the entire blade. Only the AoA determines the flow-field and thus the aerodynamic forces in 3D.Moreover, different operative conditions, which lead to similar AoAs, do not directly influence the non-dimensionalized aerodynamic forces.

In Fig. 3 the suction side of the blade is highlighted. Pressure contours and wall shear streamlines are coupled in order to present the strong relationship between flow-field and pressure distribution.

The analogy in both pressure and streamline distributions for A and B conditions is immediately evident. This confirms the fact that the rotational speed does not substantially influence the flow-field and the pressure distribution. Furthermore, it is interesting to notice that in both conditions the boundary layer presents a strong radial component starting from the inner blade and developing near the trailing edge region.

	Condition **A**	Condition **B**
3D	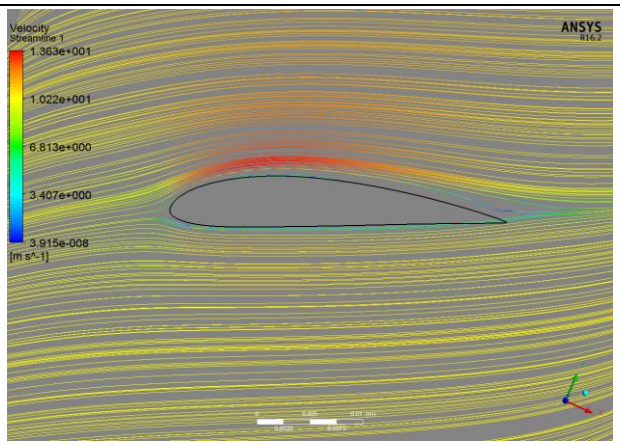	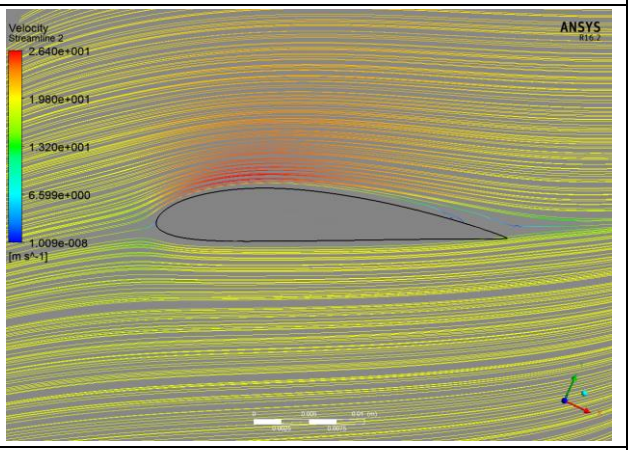
2D	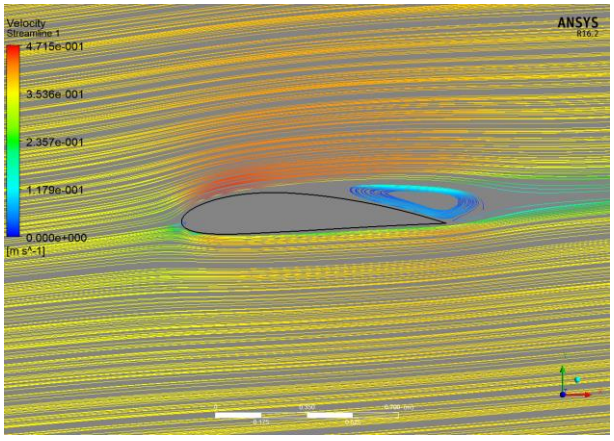	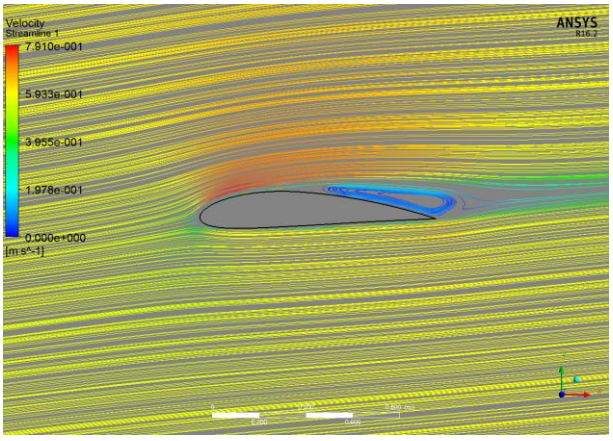
3D	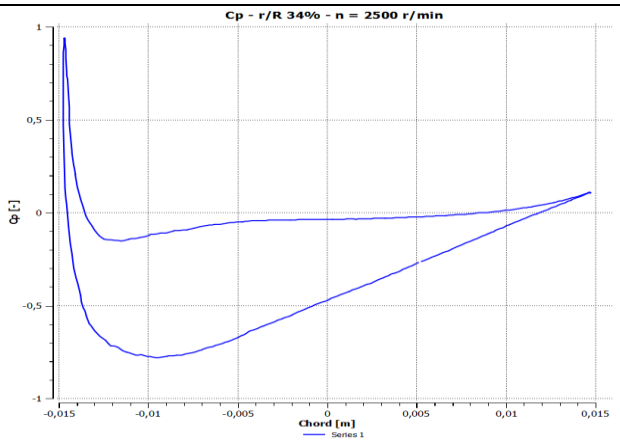	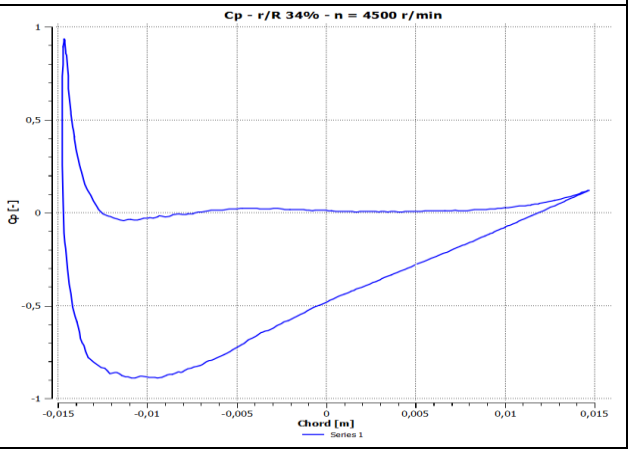

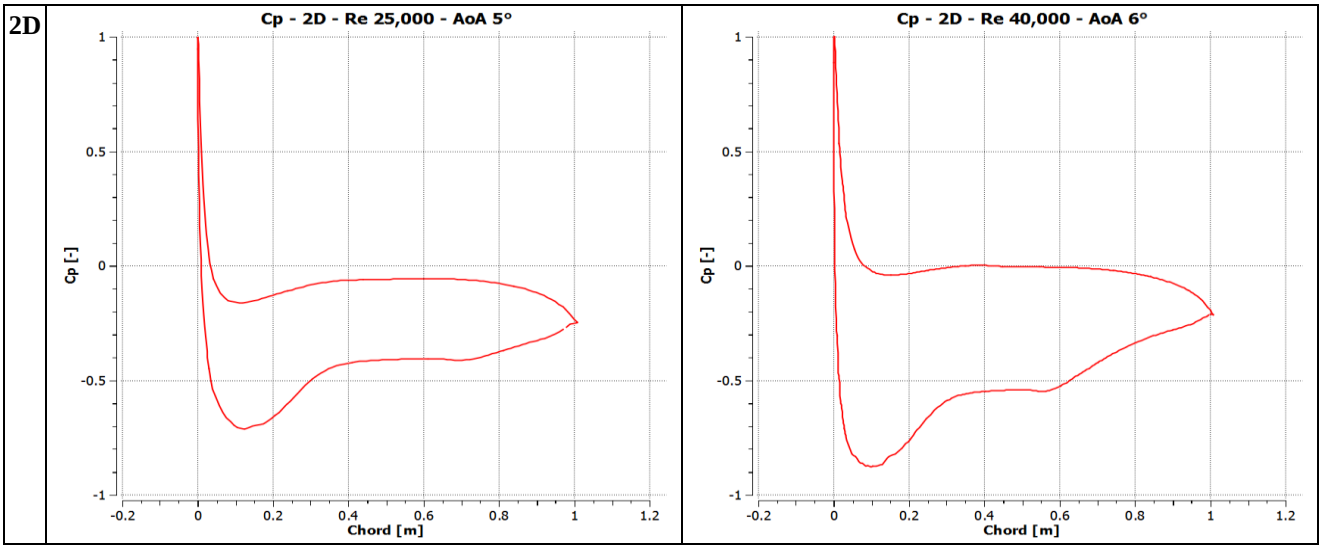

Figure 1: 3D – 2D Surface streamlines and C_p comparison at r/R 34%

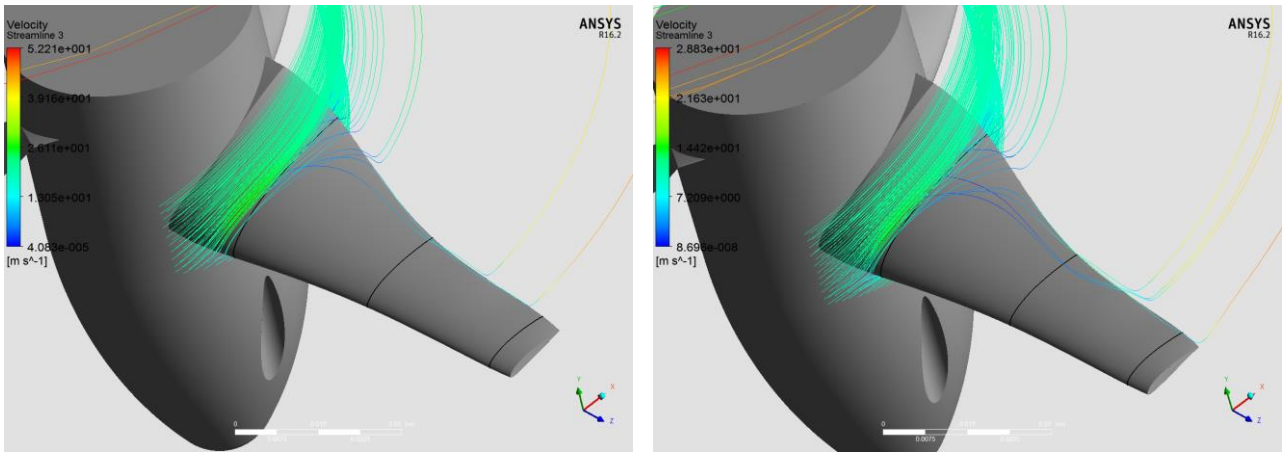

Figure 2: 3D streamlines at r/R 34% for condition A (left) and condition B (right)

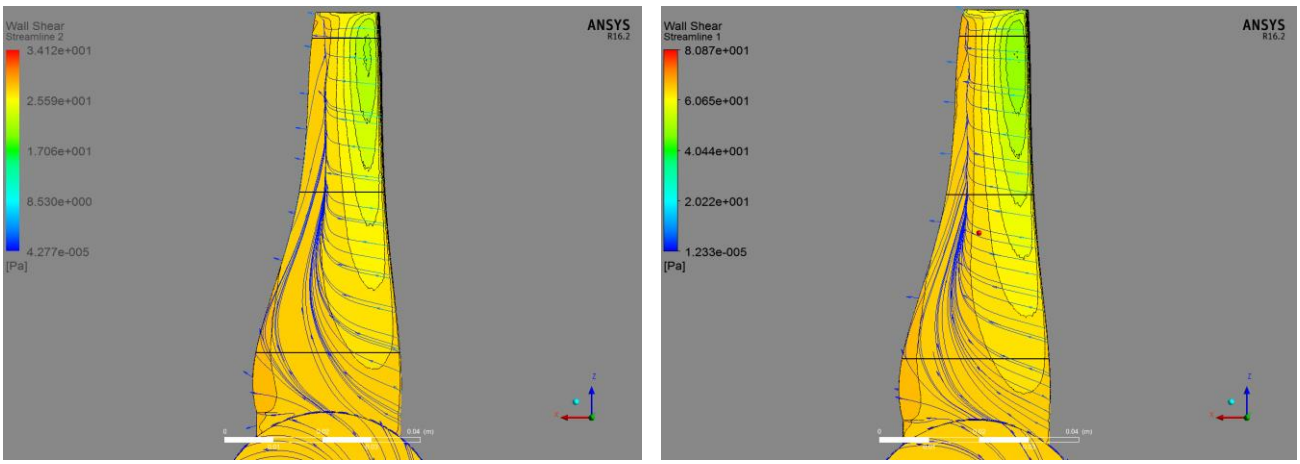

Figure 3: Pressure contours and wall shear streamlines on suction side for condition A (left) and B (right)

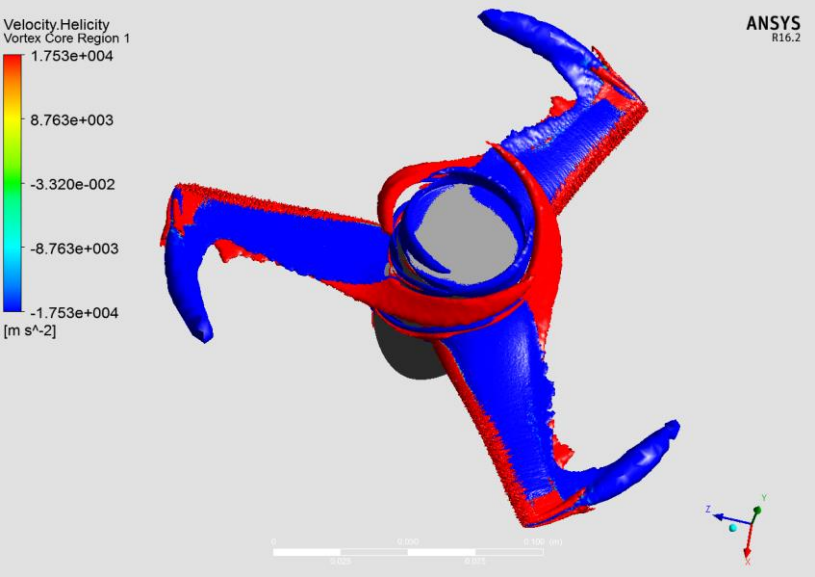

Figure 4: Vortex core region for B condition

In conclusion, the comparison between 2D and 3D results at low AoAs in attached flow conditions demonstrates some differences in the fluid dynamic behavior. However, from the proposed analysis, it is evident that this does not lead to substantial differences between 2D and 3D aerodynamic coefficients and, moreover, the suppositions from scientific literature, that the rotation leads to a boundary layer reattachment and to a stall delay, is very close to reality.

Lastly, a vortex core region post-processing image of the entire rotor is presented in Fig. 4. This technique allowed for the detection of coherent helical structures which strongly affect the rotor flow-field in comparison to simple 2D flows. Also in this case there are no substantial differences between A and B conditions, thus only one image is attached. The coherent swirling structure near the tip, which is the widely known tip vortex, is highly noticeable. No other coherent structures are evident.

Medium AoAs analysis: maximum lift condition

The medium AoA condition is the most interesting one because the rotational effects reach their maximum thus allowing for an adequate comprehension of the complex mechanism induced by rotation. Also in this case, two different operative conditions were analyzed as reported in Tab. 2.

The analyzed conditions are extremely different although they lead to similar AoAs and Tip Speed Ratios (TSR). Condition C is characterized by V_w = 10 m/s and n = 1,500 r/min while in condition D, V_w = 30 m/s and n = 4,500 r/min.

Table 2: Extrapolated data for different 2D – 3D conditions for maximum lift condition

CFD 3D						
Wind and rotational speed	**V_w = 10 – n = 1,500 (C)**			**V_w = 30 – n = 4,500 (D)**		
r/R [%]	34	65	95	34	65	95
AoA [deg]	37.2	30	24.7	37.5	29.9	24.6
C_l [-]	1.94	1.05	0.64	1.96	1.07	0.67
C_d [-]	1.1	0.53	0.24	1.03	0.49	0.22
MVR	2.2	1.53	1.42	2.23	1.54	1.48
Mean Re	22,000			65,000		
CFD 2D						
AoA [deg]	37	30	25	37	30	25
C_l [-]	0.87	0.83	0.79	0.87	0.83	0.79
C_d [-]	0.66	0.49	0.38	0.66	0.49	0.38
MVR	1.29	1.28	1.26	1.29	1.28	1.26

Starting again from the inner blade analysis (r/R 34%) a strong augmentation in lift and drag coefficients is evident in Tab. 2, further confirming the fact that the inner blade is where the rotational effects reach their maximum. Specifically, the calculated 3D lift coefficient is more than twice the 2D lift coefficient and no differences are detected between C and D conditions. This further demonstrates that the rotational effects are substantially not dependent on wind or rotational speed and thus on the Reynolds number either.

The force augmentation regards the entire resultant of the aerodynamic forces as the drag coefficient is slightly increased as well.

Only the AoA and, therefore, the particular flow-field condition, lead to the generation of a phenomenon which, acting in the inner blade, determines a force augmentation of such strength. Indeed, in Fig. 5, a noticeable equality of the flow-field for both C and D 3D conditions is evident from the streamline analysis. It is clear how the rotation modifies the flow-field, compared to the 2D condition. All the separated area, which in 2D generates two counter-rotating vortices, is subjected to the rotation effects which push down and flatten the stall vortices. Such a drastic effect is clearly expressed by a strong depressurization of the suction side of this part of the inner blade as can be evaluated in C_p charts in Fig. 5. While the pressure distribution on the pressure side is almost the same in both 2D and 3D conditions, only the suction side is affected by such a strong depressurization. The pressure coefficient reaches a value of -7 near the leading edge.

However, the depressurization is evident in the entire chord-wise direction as the C_p value is below -1 for the largest part of the chord. The rotation induces a strong flow acceleration near the leading edge, therefore the MVR is equal to 2.2, while in 2D the MVR is only 1.29. This means that the flow in 3D is accelerated 2.2 times the undisturbed velocity while in 2D only 1.29 times. This is due to the forces generated by rotation, as will be demonstrated hereinafter. These forces act on the entire separated layer modifying and strongly accelerating the flow on the suction side of the inner blade.

	Condition **C**	Condition **D**
3D	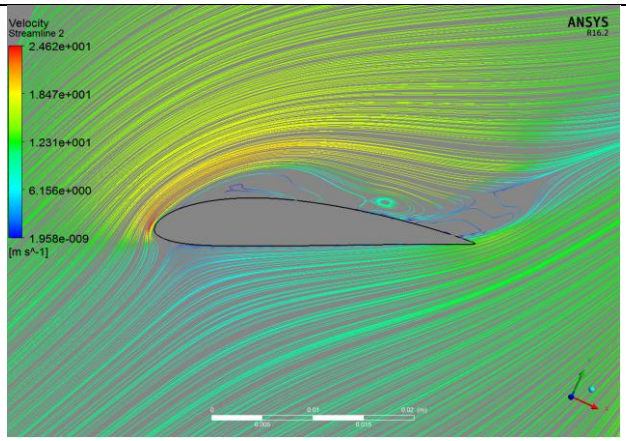	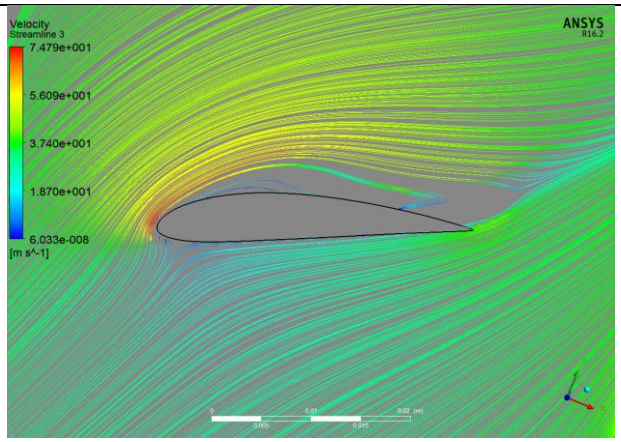
2D	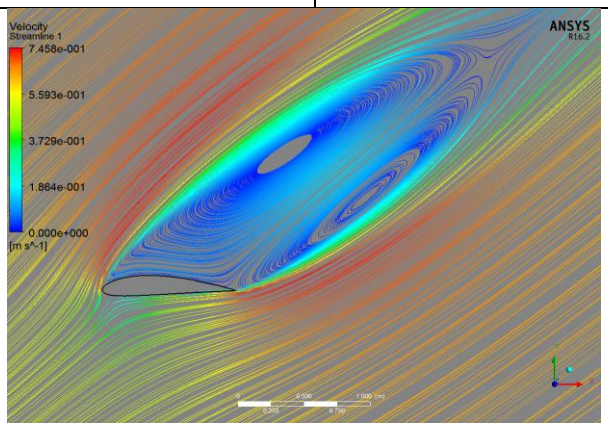	

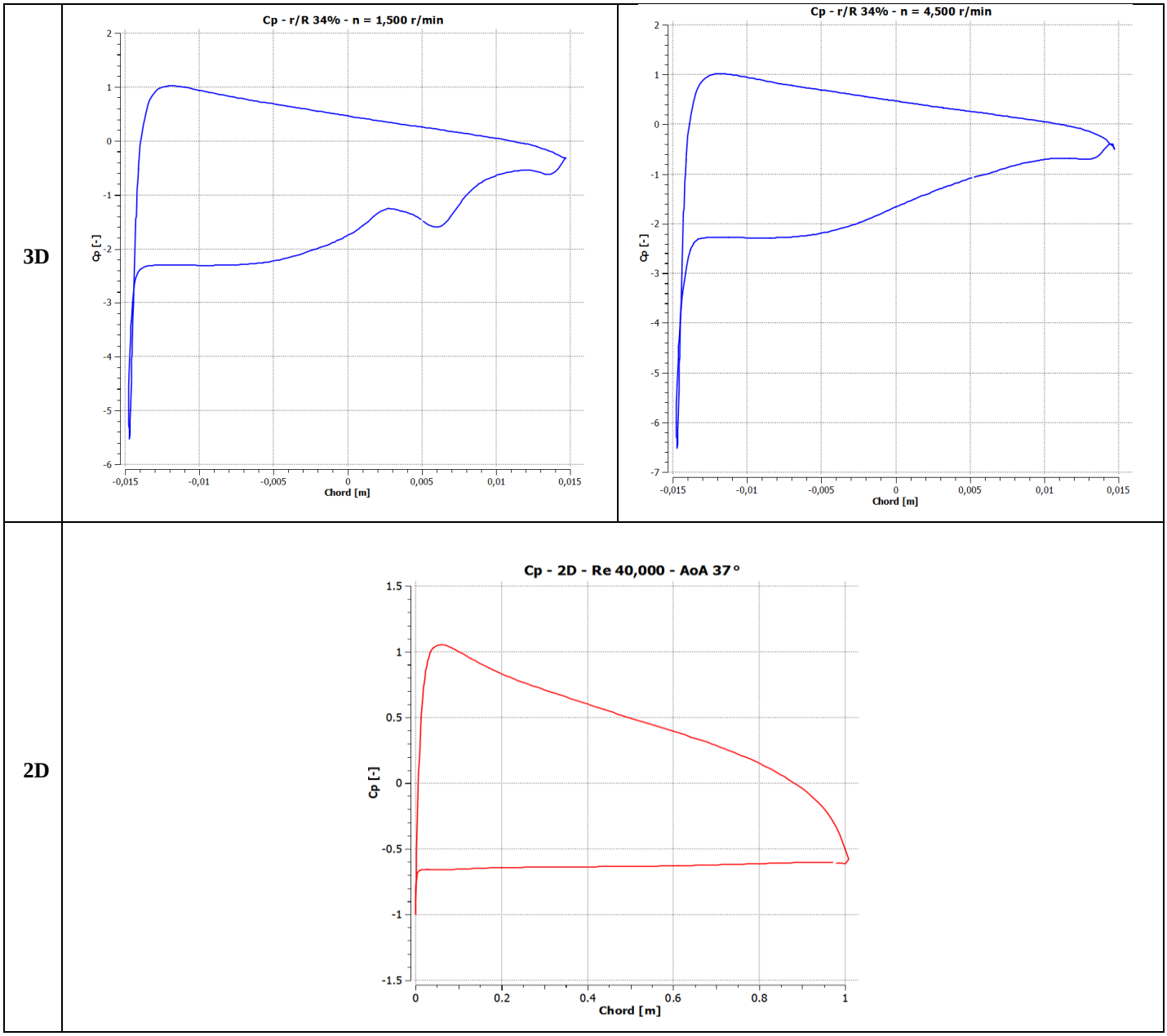

Figure 5: 3D – 2D Surface streamlines and C_p comparison at r/R 34%

As evidenced in Fig. 6, a 3D coherent helical structure develops from the inner blade in an identical way for C and D conditions. The swirling structure is responsible for the flow acceleration and, consequently, for the strong depressurization. The rotational forces act with a precise balance tangling the flow in a helical structure and, like in a tornado, the flow strongly accelerates and depressurizes the entire separated layer. It is also interesting to notice that the helical structure is superimposed to an intense radial flow, directed toward the tip, which is in close proximity to the blade surface. The flow at a certain distance higher from the blade is instead deflected toward the hub. The helical vortex, once detached from the inner blade, develops all the way up to mid-blade, where leaves it.

The above is confirmed in Fig. 7 where wall shear streamlines show the onset of the helical vortex in the lower boundary layer near r/R 34% section. Furthermore, the depressurization generated by this helical structure is demonstrated by the pressure contours, which clearly follow the wall shear streamlines. Therefore, a big portion of the inner blade is subjected to a very strong depressurization. Thus the aerodynamic forces are considerably augmented. The generation of the helical vortex in the inner blade is therefore to be considered the most responsible factor for the rotational augmentation.

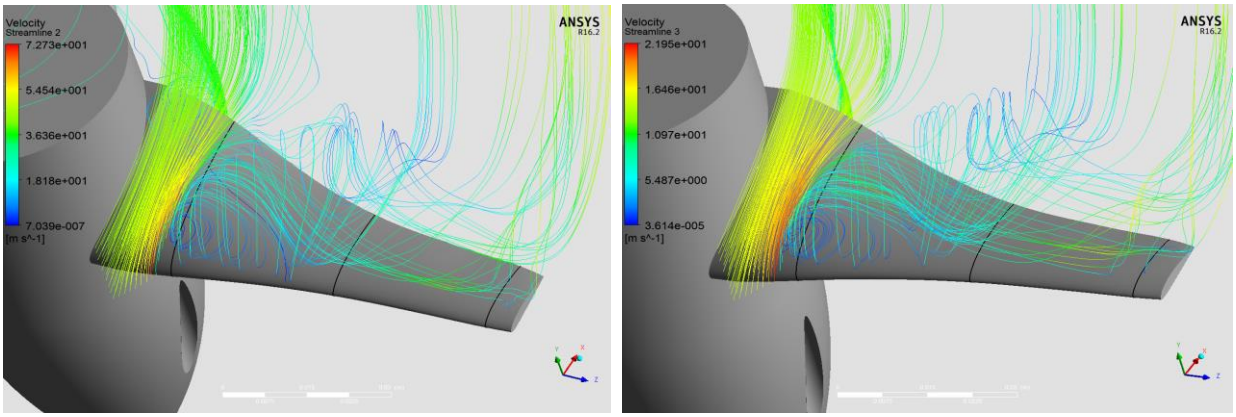

Figure 6: 3D streamlines at r/R 34% for condition C (left) and condition D (right)

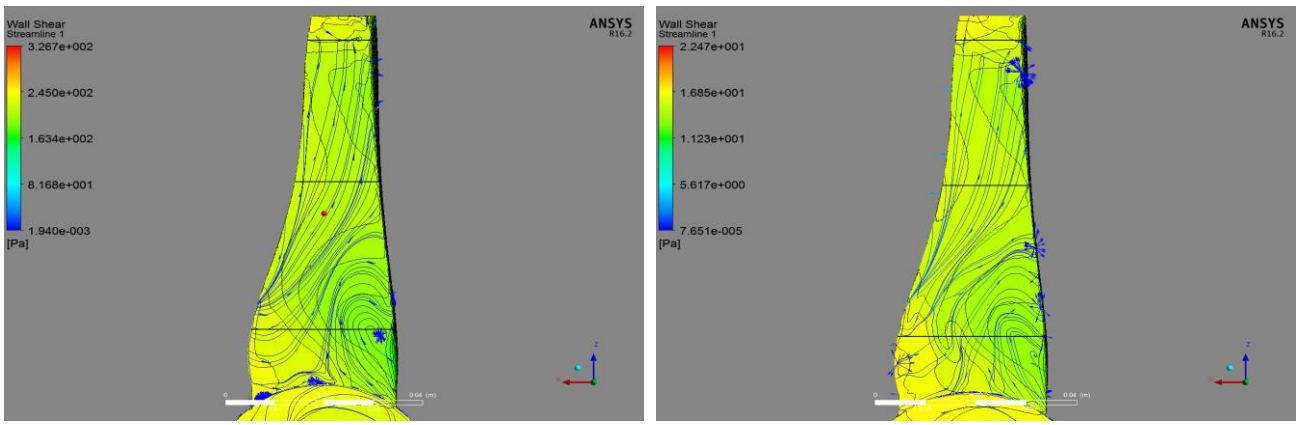

Figure 7: Pressure contours and wall shear streamlines on suction side for condition C (left) and D (right)

Despite the fact that, at medium blade (r/R 65%), the centrifugal and Coriolis forces are certainly higher, the absence of a helical structure leads to a 3D flow-field similar to that in the 2D condition, as reported in Fig. 8. A strong radial flow is however present close to the blade surface while the upper separated area is almost comparable to 2D. The rotational augmentation is considerably reduced. The MVR demonstrated, however, higher flow acceleration in the suction side than in 2D and this explains the higher lift and drag coefficients. Indeed, from the 2D - 3D C_p comparison in Fig. 8, the pressure distribution is truly similar and it is typical of a stalled condition. Only a high depressurization is detectable in 3D near the leading edge where the C_p is below 2 in both C and D conditions. Then, the pressure distribution shows a slightly lower trend than in 2D, but at the same time similar. This justifies the minor increase in lift and drag coefficients. The increase is evidently related to the flow acceleration on the suction side due to the 3D effects.

	Condition **C**	Condition **D**
3D	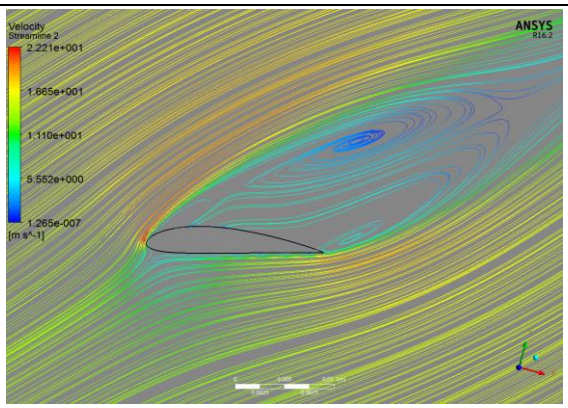	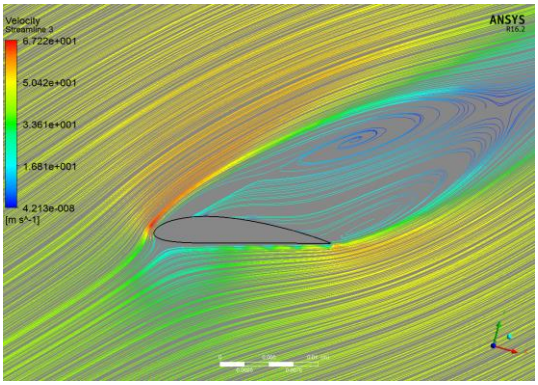

2D

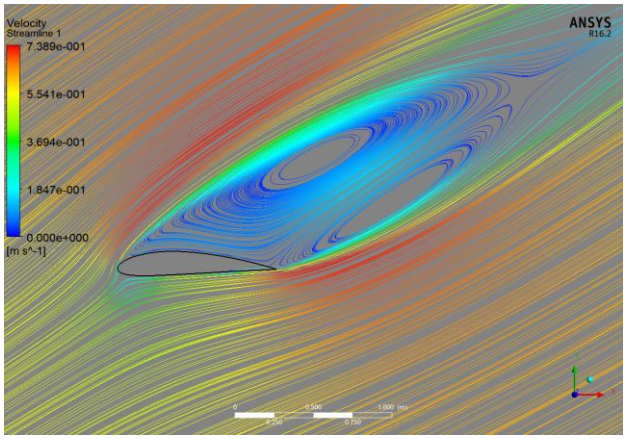

3D

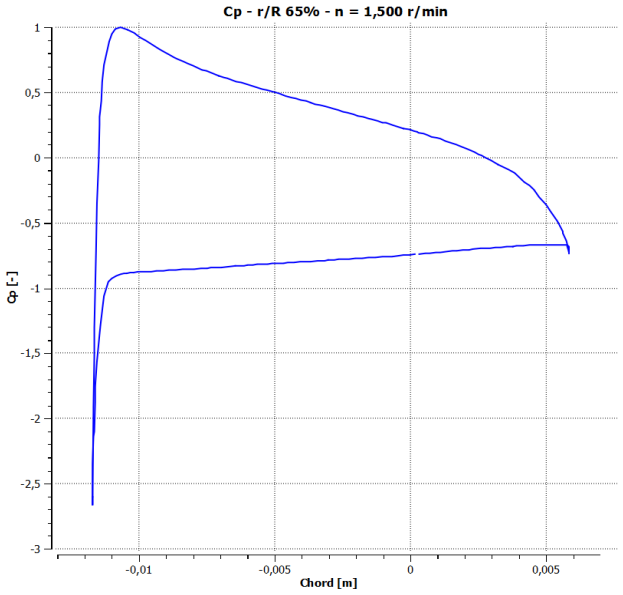

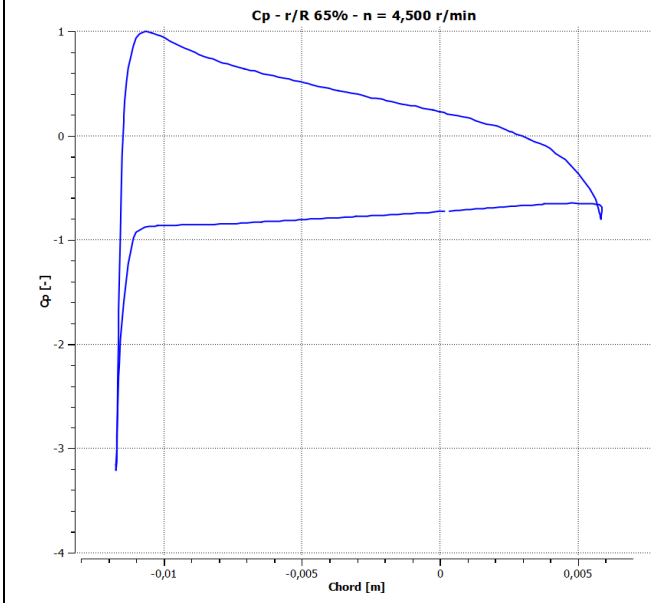

2D

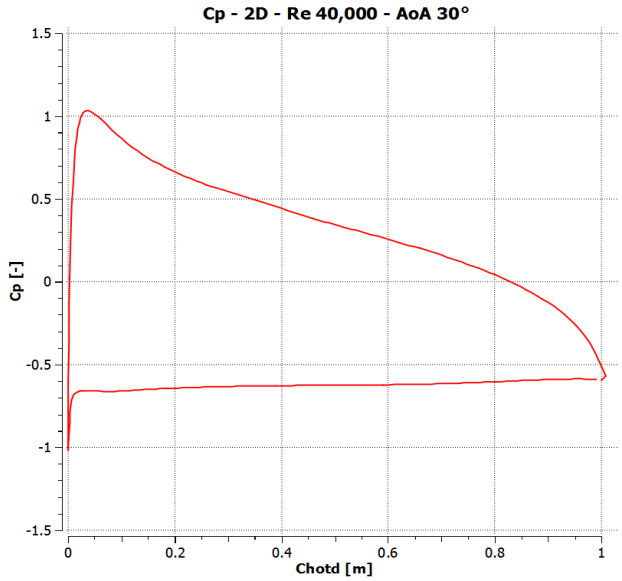

Figure 8: 3D – 2D Surface streamlines and C_p comparison at r/R 65%

The r/R 95% analysis showed similar results to that obtained at r/R 65% except for the strong effects of the tip losses as clearly evident in Tab. 2.

It is important to further analyze the rotation effect in this maximum lift condition and medium AoAs in order to improve the comprehension of the mechanism. This leads to the aforementioned strong force augmentation. In particular, it is supposed that the onset of a helical structure on the inner blade, the effects of which are similar to those of a tornado in terms of pressure drop, is mainly responsible for the depressurization and lift and drag augmentation. Thus, the hypothesis proposed in the scientific literature, which states that is the simple radial flow and the centrifugal and streamwise Coriolis forces which cause the rotational augmentation, seems to be too restrictive in light of these new considerations.

In order to highlight the effects generated by the helical vortex, the helicity function is introduced. Helicity (H) is defined as the integrated scalar product of velocity field $\boldsymbol{u}$ and vorticity field $\boldsymbol{\Omega}$:

$$H = \int (\boldsymbol{u} \cdot \boldsymbol{\Omega}) dV \qquad (2)$$

In (2), scalar product between $\boldsymbol{u}$ and $\boldsymbol{\Omega}$ is the helicity density.

As reported in scientific literature, helicity is useful in detecting helical structures and their strength [8 – 13]. The great advantage of helicity is that both its magnitudes and sense are meaningful. High values of helicity reflect high values of speed and vorticity when the relative angle between them is small. The sign of helicity density is determined by the sign of the cosine of the angle between the velocity and vorticity vectors. Thus, the sign of the helicity indicates the direction of swirl of the vortex relative to the streamwise velocity component. Both the relative size of the helicity and the changing of the swirl direction, which is emphasized by graduation in color for magnitude and by different colors for positive or negative values, clearly distinguish between primary and secondary vortices in the graphical representation. Therefore, through the use of post processing images of helicity, pressure distribution and streamlines, it is possible to demonstrate how the development of an helical vortex influences the flow-field and the aerodynamic forces on the rotating blade.

The helicity contours in Fig. 9 are obtained on five sections perpendicular to the radius and a planar section parallel to the radius. Two main helicity sources are evident. The first one, in the inner section, reaches its maximum on the surface perpendicular to the radius. This indicates that a strong helical vortex, detached from the blade, developed approximately in the radial direction. However, another interesting helical structure is detectable near the r/R 80% section. This time the vortex core is approximately pointed in the streamwise direction. Other sources of helicity are present near the leading and trailing edge due to the flow acceleration and vorticity production in that area. However, they are not directly related to helical vortices.

In Fig. 10 the comparison between helicity contours, streamlines and pressure distribution emphasizes the fact that, in the area in which the helical vortex is developed, a strong depressurization occurs over the blade. This is further confirmed in Fig. 11 where the pressure contours in a section perpendicular to the blade show that the areas where the pressure are lower are exactly where the helical vortices develop, that is near r/R 34% and r/R 80%. The pressure distribution on the pressure side is instead evidently quite regular.

The depressurization generated by helical vortices clearly increases the aerodynamic forces on the blade. Indeed, while the AoA decreases along the blade, the lift and drag coefficients present a slight increase at near r/R 80%, as can be seen in the chart presented in Fig. 12. The correspondence between Fig. 11 and Fig. 12 is evident. In the inner section, the lower pressure caused by the helical vortex, leads to the aforementioned strong increase in lift and drag coefficients.

Finally, in Fig. 13, the iso-surface of the vortex core region shows three main helical structures. The first one detaches from the inner blade, the second one detaches at r/R 80% and the third one is the widely known tip vortex.

It is thus demonstrated that the development of helical structures lead to a strong blade depressurization. This is responsible for the rotational augmentation experienced at this medium AoA condition. The onset of the helical structures is not dependent on the rotational and wind speed and depends only on the AoA, as no differences are evident between C and D conditions. The specific AoA leads to a force equilibrium that triggers the onset of the helical vortex in the inner blade as will be shown in section 3. Furthermore, the onset of the helical structures is not to be considered abrupt. The strength and the intensity of the helical vortex gradually increase as the AoA increases. After the maximum lift, further increments of the AoA lead to a gradual decrease in the helical vortex intensity, thus the depressurization and the aerodynamic forces are reduced as well. At higher AoAs, the boundary layer adverse pressure gradient, in the chordwise direction, prevails and the flow definitely separates. This is demonstrated in the next sub-section.

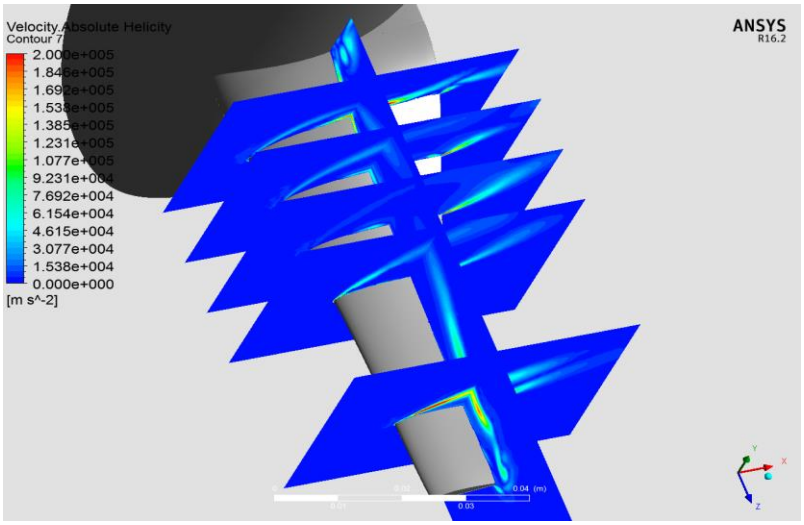

Figure 9: Helicity contours on perpendicular section over a blade for C condition

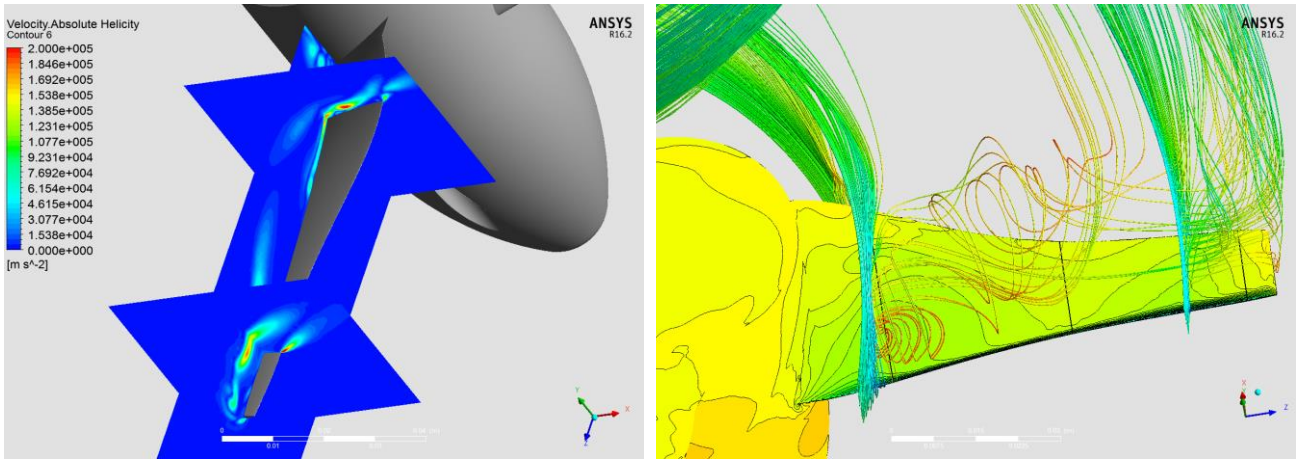

Figure 10: Helicity contours on blade section (left), 3D streamlines at r/R 34% - r/R 80% and pressure contours (right) (condition C)

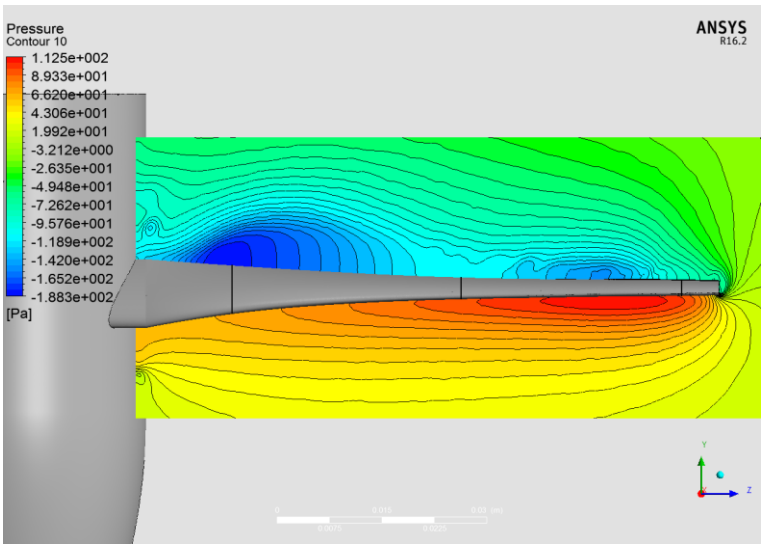

Figure 11: Pressure contours in a section perpendicular to the blade for C condition

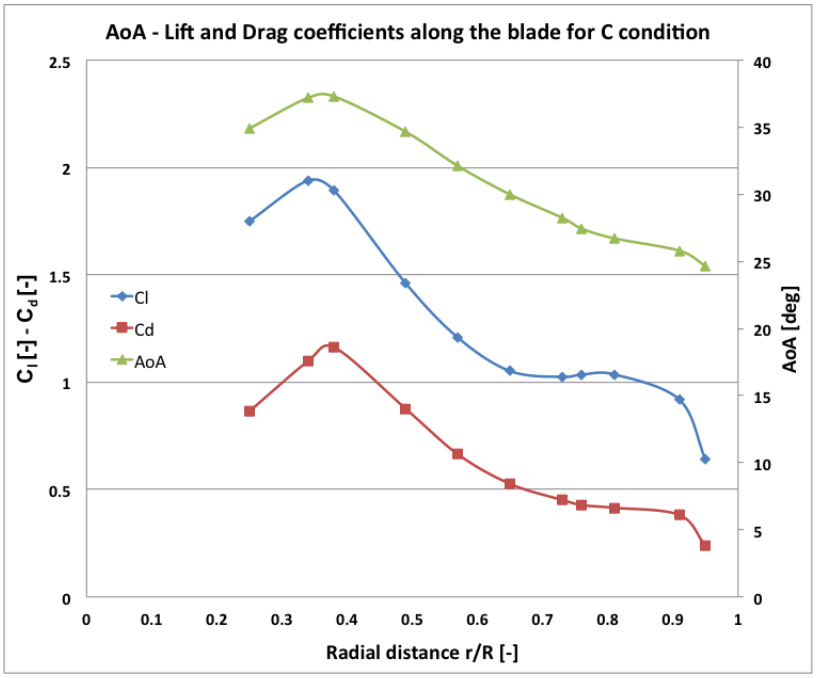

Figure 12: AoA, lift and drag coefficients radial distribution for C condition

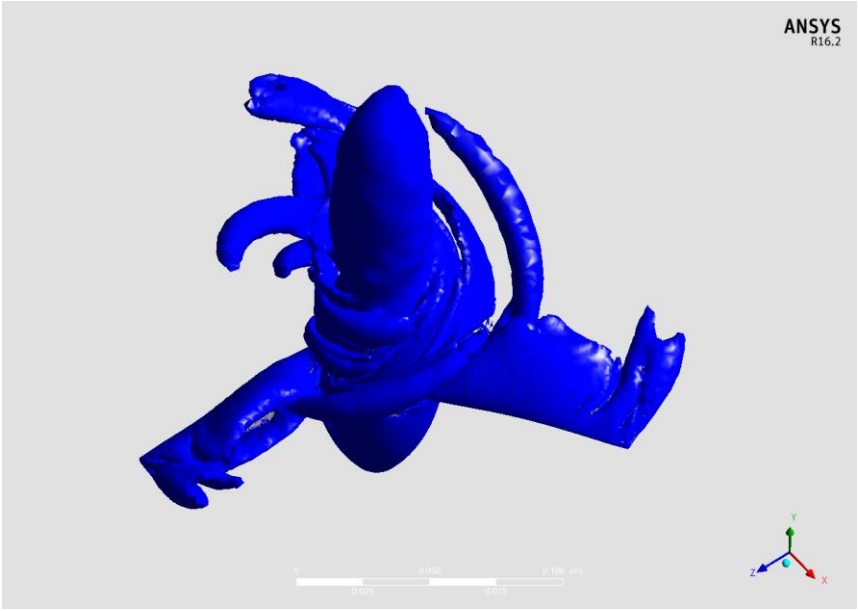

Figure 13: Vortex core region for C condition

High AoAs analysis: fully stalled conditions

In order to complete the flow-field study, a fully stalled condition is briefly analyzed. As previously seen, no differences are detectable between conditions which lead to a similar AoA distribution along the blade. Thus only one condition (Condition E: V_w = 30 m/s, n = 1,000 r/min) is presented and compared to 2D results. In Tab. 3 a substantial equivalence between calculated 3D - 2D data is evident. It is clear that the 3D rotational augmentation is definitely not present and the aerodynamic forces are comparable to 2D. The MVR shows that the flow acceleration is not so high due to the fact that the 3D effects do not strongly affects the flow-field.

Indeed, at r/R 34% in Fig. 14 a similar full separation is evident in both 2D and 3D cases. However, while in 2D, two counter rotating vortices characterize the suction side flow-field, the flow in 3D is distorted and the secondary vortex, detached from the trailing edge, is almost absent. What is remarkable is that, in this case, no helical vortex develops in the inner blade thus no strong flow acceleration, or

depressurization are detected. This is due to the fact that the adverse pressure gradient in the stream-wise direction prevails on the rotational effects and the flow separates in a way similar to 2D. The C_p charts in Fig. 14 confirm a substantial equality in the pressure distribution between 2D and 3D conditions thus the aerodynamic forces are almost similar as well. Similar considerations can be made for r/R 65% and r/R 95% therefore the analysis is omitted.

Table 3: Extrapolated data for different 2D – 3D conditions for fully stalled condition

	CFD 3D			**CFD 2D**		
Wind and rotational speed	**V_w = 30 – n = 1,000 (E)**			-		
r/R [%]	34	65	95	34	65	95
AoA [deg]	60.1	63.9	63.3	60	63.5	63.5
C_l [-]	0.84	0.66	0.6	0.795	0.73	0.73
C_d [-]	1.32	1.22	1.07	1.3	1.37	1.37
MVR	1.49	1.41	1.37	1.38	1.38	1.38
Mean Re	45,000			45,000		

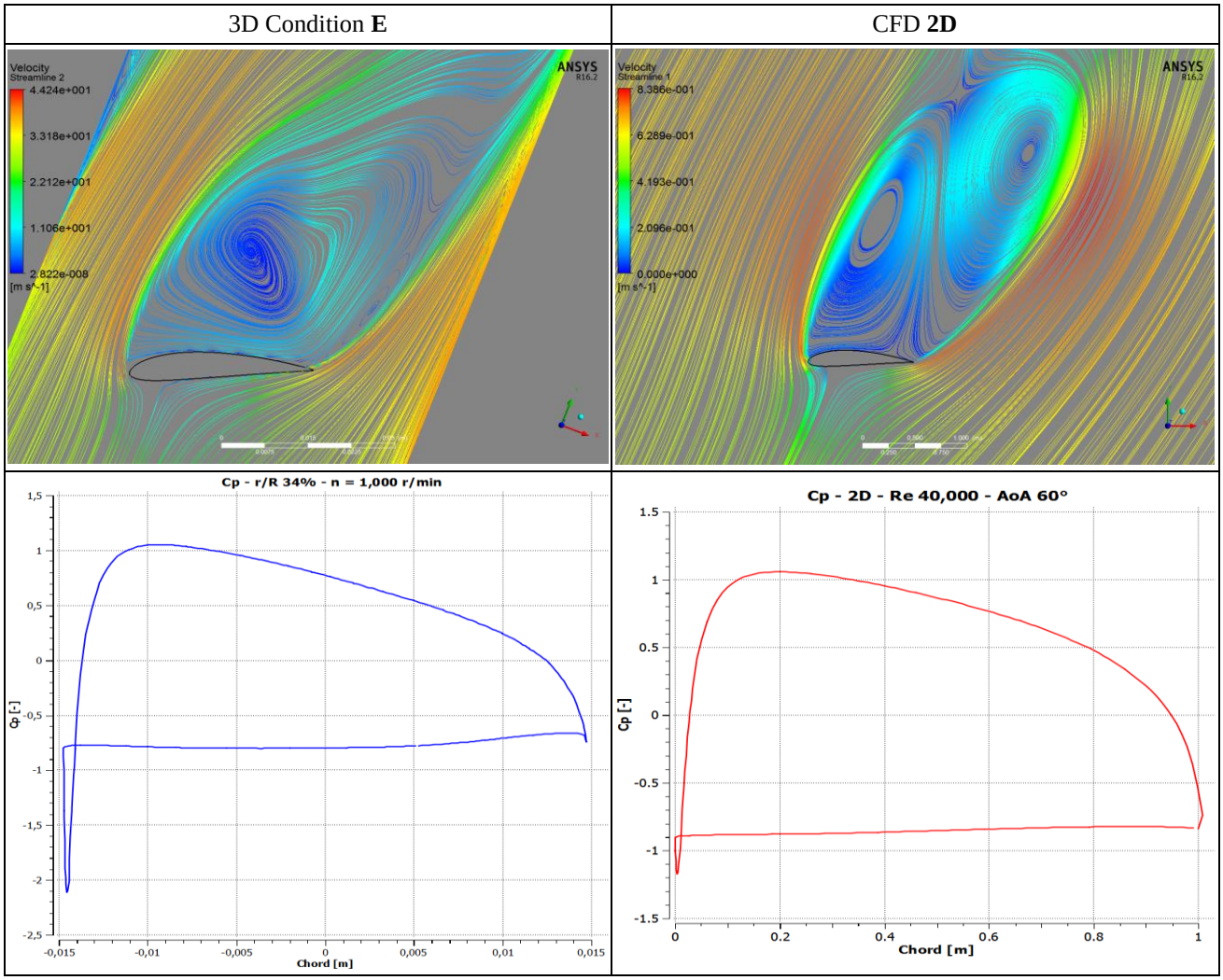

Figure 14: 3D – 2D Surface streamlines and C_p comparison at r/R 34% (condition E)

However, a radial flow is always present along the entire blade, as evidenced in Fig. 15. Here, the pressure contours and the wall shear streamlines are shown. The differences in the pressure distribution and in the flow-field between the pressure side and the suction side are emphasized. Furthermore, the pressure distribution on the suction side is almost regular without a higher depressurization area, according to a fully stalled condition. The wall shear streamlines on the suction side signals the presence of the radial flow over the blade. A radial line separates two zones: once the streams impact on the blade surface, a part goes toward the leading edge, another part goes toward the trailing edge. This is clearly related to the two distorted counter-rotating vortices that push the flow down toward the blade surface.

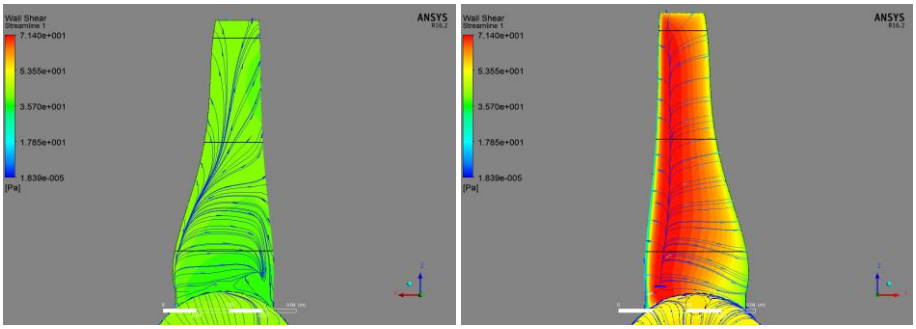

Figure 15: Pressure contours and wall shear streamlines on suction side (left) and pressure side (right)

Some considerations may be made at this point on the rotational effects. When the operative conditions lead to low AoAs and the flow is almost attached, the rotation acts generating a radial flow that stabilizes the boundary layer with at most a slight increase of the aerodynamic forces. As the AoA increases, the rotational forces act by triggering the onset of coherent helical vortices which gradually increase in intensity. The final effect is a further depressurization of the suction side of the blade. This creates a consequent increase of the aerodynamic forces, which is located above all in the inner blade, where the force balance creates the conditions for the helical vortex to develop. This effect reaches its maximum at an AoA which is approximately equal to 35 - 37 degrees. Further increments of the AoA gradually reduce the rotational augmentation as the helical vortex loses intensity due to the higher adverse pressure gradient in the streamwise direction. At an AoA > 55/60°, the rotational forces are no longer sufficient to overcome the adverse pressure gradient and the flow definitely separates. In this fully stalled condition, the 3D aerodynamic forces are slightly reduced compared to the 2D one. In this process, the influence of wind and rotational speed is marginal and related only to the AoA distribution that they generate over the blade. So, the Reynolds number effect is quite limited as well. Only the AoA leads to a particular flow-field and force balance that guides this phenomenon. The above is useful in order to improve the comprehension of the rotational augmentation and to give a clear explanation on why and how the rotational augmentation takes place. In the next section the force analysis and the 3D fixed wing simulation results will clarify the aforementioned assumptions.

FORCE ANALYSIS AND FIXED BLADE RESULTS

Force analysis

The rotation effects on the 3D flow-field have been widely shown. In particular, in section 2.2 it is evidenced that a helical vortex is mainly responsible for the strong depressurization of the inner blade. In the reviewed literature only the effects of a simple radial flow are highlighted and most of the rotational augmentation is ascribed to the chordwise component of the Coriolis force. This is not entirely accurate because in 2.2 it is demonstrated that, at a certain axial distance from the blade, the flow is deflected toward the hub while, in close proximity to the blade, the flow is essentially radially directed. This means that in the blade proximity the forces directed toward the tip prevail while at a certain distance there must be strong forces directed toward the hub. It is just the reversal of the forces, and the shear related to it, that trigger the onset of the helical vortex with all the aforementioned consequences like flow deflection, strong depressurization and finally rotational augmentation. In order to demonstrate these assumptions, the forces acting at different chord positions and radial stations are analyzed hereinafter. Specifically, the analysis for C and D conditions are presented and compared with the attached flow condition A. Then the fixed blade simulation results, described in part I of this work, will finally confirm the hypotheses from the force analysis, leading the way for a new and better comprehension of the rotational augmentation phenomena.

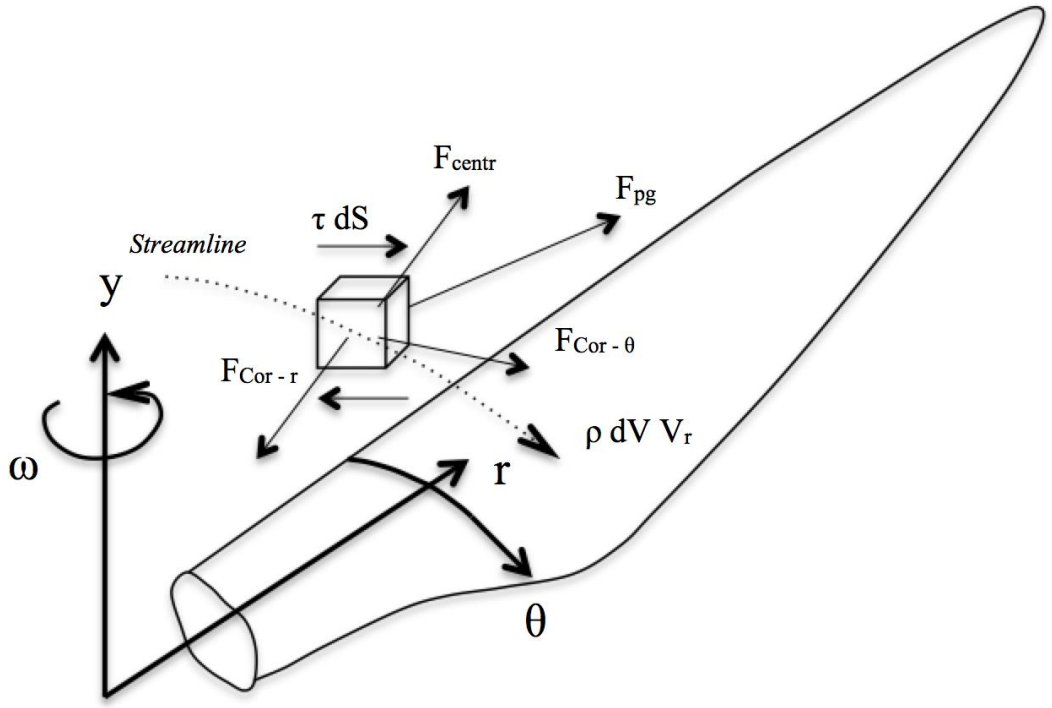

Figure 16: Cylindrical coordinates in a rotating frame of reference and forces acting on a fluid element

In order to analyze the forces in a rotating frame of reference, the equation of motion must be written in cylindrical coordinates using the system of Fig. 16 [14], where θ is the azimuth direction, r the radial direction, y the axial direction and ω the rotational speed.

$$\frac{\partial v_\vartheta}{r\partial\vartheta}+\frac{\partial v_y}{\partial y}+\frac{\partial v_r}{\partial r}+\frac{v_r}{r}=0 \quad (3)$$

$$\frac{\partial v_\vartheta}{\partial t}+\frac{v_r\partial v_\vartheta}{\partial r}+\frac{v_\vartheta\partial v_\vartheta}{r\partial\vartheta}+\frac{v_r v_\vartheta}{r}+\frac{v_y\partial v_\vartheta}{\partial y}=F_\vartheta-\frac{\partial p}{\rho r\partial\vartheta}+\frac{\mu}{\rho}\left(\frac{\partial^2 v_\vartheta}{\partial r^2}+\frac{\partial v_\vartheta}{r\partial r}+\frac{\partial^2 v_\vartheta}{r^2\partial\vartheta^2}+\frac{\partial^2 v_\vartheta}{\partial y^2}\right) \quad (4)$$

$$\frac{\partial v_r}{\partial t}+\frac{v_r\partial v_r}{\partial r}+\frac{v_\vartheta\partial v_r}{r\partial\vartheta}-\frac{v_\vartheta^2}{r}+\frac{v_y\partial v_r}{\partial y}=F_r-\frac{\partial p}{\rho\partial r}+\frac{\mu}{\rho}\left(\frac{\partial^2 v_r}{\partial r^2}+\frac{\partial v_r}{r\partial r}+\frac{\partial^2 v_r}{r^2\partial\vartheta^2}+\frac{\partial^2 v_r}{\partial y^2}\right) \quad (5)$$

$$\frac{\partial v_y}{\partial t}+\frac{v_r\partial v_y}{\partial r}+\frac{v_\vartheta\partial v_y}{r\partial\vartheta}+\frac{v_y\partial v_y}{\partial y}=F_y-\frac{\partial p}{\rho\partial y}+\frac{\mu}{\rho}\left(\frac{\partial^2 v_y}{\partial r^2}+\frac{\partial v_y}{r\partial r}+\frac{\partial^2 v_y}{r^2\partial\vartheta^2}+\frac{\partial^2 v_y}{\partial y^2}\right) \quad (6)$$

(3), (4), (5), (6) are the continuity equation and the Navier-Stokes equations in cylindrical coordinates. Here, $\mathbf{v} = (v_\theta, v_r, v_y)$ is the velocity vector, p is the pressure, ρ is the density, μ the dynamic viscosity and $\mathbf{F} = (F_\theta, F_r, F_y)$ the external force per unit mass. In particular, in this rotating frame of reference the **F** components are:

$$F_\vartheta = F_{Cor-\vartheta} = 2\omega v_r \quad (7)$$

$$F_r = F_{centr} + F_{Cor-r} = \omega^2 r - 2\omega v_\vartheta \quad (8)$$

$$F_y = 0 \quad (9)$$

Equations (7), (8), (9) refer to Fig. 16 for the notation. Specifically, in Fig. 16 a fluid element, travelling along a streamline that approach the leading edge of the inner blade, is evidenced. The main forces of interest for the present analysis are highlighted. Two more forces are in addition to forces (7) and (8): the pressure gradient force F_{pg} and the shear force τdS as well as the momentum of the fluid element denoted by ρ dV $\mathbf{V_r}$, being dV the infinitesimal volume and $\mathbf{V_r}$ the relative velocity vector of the fluid element.

The pressure gradient per unit mass and the shear force are expressed as follows:

$$\boldsymbol{F_{pg}} = -\frac{\nabla p}{\rho} \quad (10)$$

$$\boldsymbol{\tau} dS = \mu\,\nabla v\, dS \quad (11)$$

Therefore, summarizing, a fluid element, which is approaching the leading edge of the blade, is subjected to the external forces (7), (8), (9) due to rotation and to the (10), (11) inherently related to the fluid dynamics. Moreover, while in (8) F_{centr} is always directed toward the tip, the versus of $F_{Cor-\theta}$ in (7) and F_{Cor-r} in (8) depends on the versus of v_r and v_θ, according to the frame of Fig. 16. If v_r is positive, that is directed toward the tip, $F_{Cor-\theta}$ is positive and directed toward

the trailing edge, otherwise $F_{Cor-\theta}$ is directed toward the leading edge. In the same way, if v_θ is positive F_{Cor-r} is negative and directed toward the hub while if v_θ is negative, that is when the flow recirculates toward the leading edge, the radial component of the Coriolis force, F_{Cor-r} is positive and directed toward the tip. It is important to keep the above information in mind for the following considerations. In the literature, only F_{centr} and $F_{Cor-\theta}$ are taken into account when the rotational augmentation is explained. The radial component of the Coriolis force, F_{Cor-r}, is always neglected. The strong effect of F_{Cor-r}, is instead demonstrated hereinafter and is of the utmost importance as in (8) the minus can completely modify the assumptions made in the literature.

A quantitative evaluation of (8) was carried out for conditions A, C and D comparing the results in order to demonstrate the differences between an attached flow and a maximum augmentation condition. This also explains the reason why very different operative conditions (C and D) lead to the same flow-field behavior and aerodynamic force augmentation. The limited effect of $F_{Cor-\theta}$ as well as how often the results are different to that supposed in the literature, is demonstrated. The influence of the pressure gradient and the shear forces is strong and essential but it is not possible to easily evaluate it with a CFD analysis. Only qualitative considerations are thus made on (10) and (11). However the quantitative evaluation of the radial forces is sufficient to demonstrate and justify the final considerations about the rotational augmentation.

In order to extrapolate the radial component of the Coriolis force, the circumferential velocity profile v_θ is obtained using ANSYS turbo Post. The velocity is calculated along a line, which is orthogonal to the blade at three chord positions: near the leading edge (**L**), at a medium chord (**M**) and near the trailing edge (**T**). Furthermore, the calculation is repeated for the three radial stations previously mentioned (r/R 34%, r/R 65%, r/R 95%).

In the charts of Fig. 17, the radial Coriolis force, the sum of the radial Coriolis and Centrifugal forces (F_r) and the velocity v_r trends are reported. Only the data relating to the suction side are shown because the suction side is where the rotational augmentation takes place. The charts compare C and D conditions at inner blade (r/R 34%) for the three aforesaid chord locations. The forces are per unit mass thus having acceleration dimension. Clearly, the centrifugal force is a constant at each radial station thus causing a shift in the sum, as is evident in the charts.

Moreover, in Fig. 17, it is clear that the effects of the radial component of the Coriolis force F_{Cor-r} are of the utmost importance. Indeed, calculating the ratio between the maximum F_{Cor-r} and F_{centr}, the value (12) is obtained for both C and D conditions at leading edge (L).

$$\frac{\max(F_{Cor-r})}{\max(F_{centr})} = 4.3 \qquad (12)$$

A similar value can be obtained if the ratio between the maximum F_{Cor-r} and $F_{Cor-\theta}$ is calculated. The fact that the radial component of the Coriolis force is more than four times the centrifugal and azimuthal component of the Coriolis forces indicates that it is of crucial importance to take into account F_{Cor-r} when analysing the rotational augmentation. Moreover, the strong similarity between C and D conditions confirms the assumption that the rotational augmentation does not depend on rotational speed or Reynolds number but only on the AoA distribution along the blade which leads to a precise force equilibrium inside the separated layer. Indeed, what is evident in Fig. 17 is also the fact that the effect of rotational forces is not limited only to the boundary layer but is extended to the entire separated layer due to the shear forces (11) that transfer momentum to the upper separated layer and vice versa.

In detail, near the leading edge (Fig. 17 – L) the radial component of the Coriolis force prevails and strongly accelerates the flow toward the hub. Indeed, the radial velocity is entirely negative. Although in the lower boundary layer low or slight negative values of v_θ cause low values of F_{Cor-r}, the presence of an upper intense acceleration increases the shear and the flow completely deflects toward the hub. At medium chord and at trailing edge (Fig. 17 – M and T) the radial flow in the lower layers is instead forced toward the tip due to the effects of both radial forces and a strong pressure gradient. The flow here is guided by the pressure gradient that causes a recirculation with negative v_θ in the blade proximity. This pushes the flow to positive radial direction with the help of both radial forces. However, at a certain distance from the blade, the net radial force becomes negative as v_θ becomes positive. This has a marked effect on the radial velocity that quickly decreases both in M and T. Therefore, it can be assumed that, while at the leading edge the strong radial component of the Coriolis force accelerates the flow toward the hub, as long as the fluid element travels in the streamwise direction, the combined effect of the pressure gradient and azimuthal flow deceleration, (or reversion) implies a change of the force direction in the lower layers that finally lead to a strong positive radial velocity. The shear, due to the sudden change of velocity direction, like in tornadoes, is responsible for the onset of the helical vortex and ultimately for the rotational augmentation.

	Condition **C** – r/R 34%	Condition **D** – r/R 34%
L	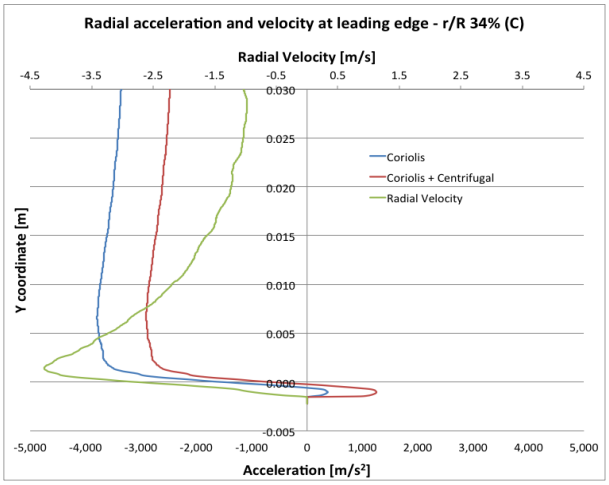	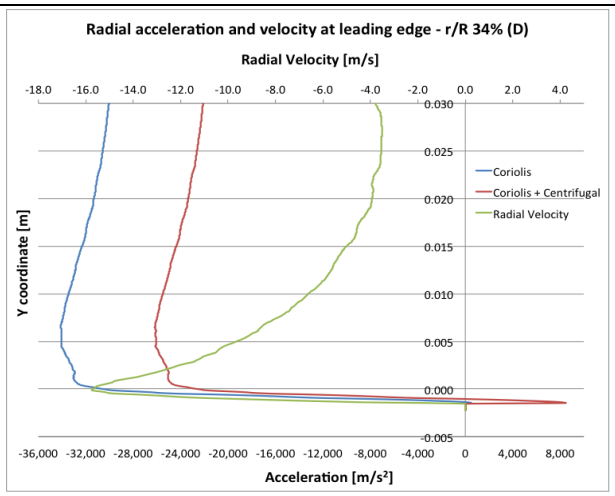
M	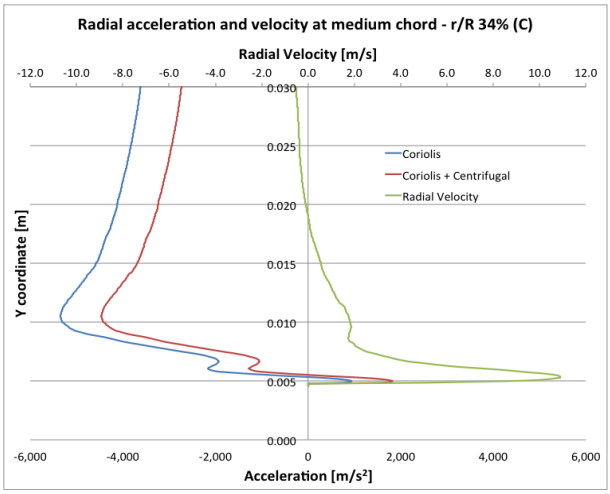	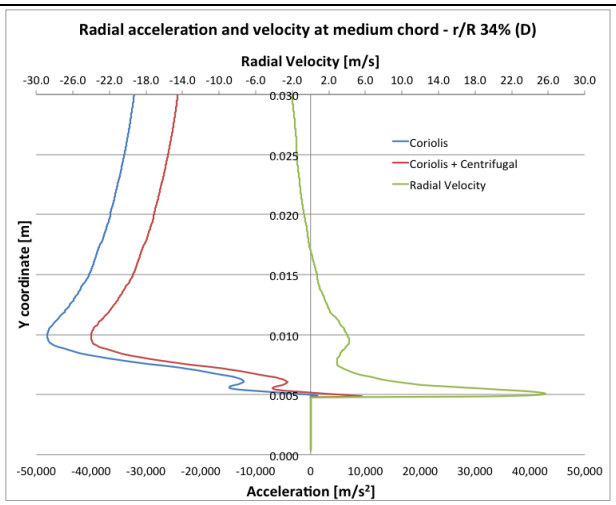
T	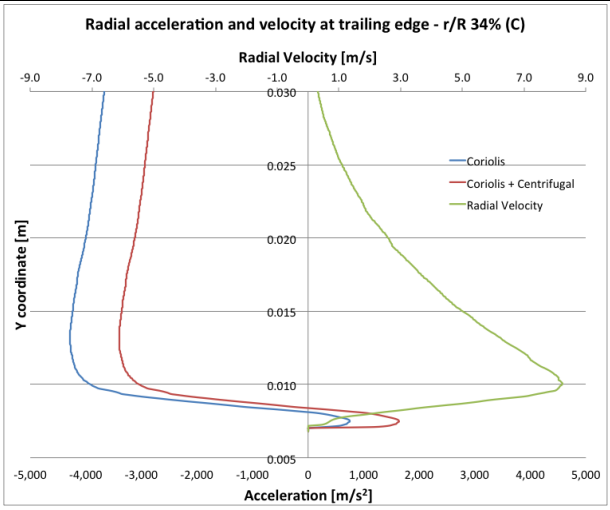	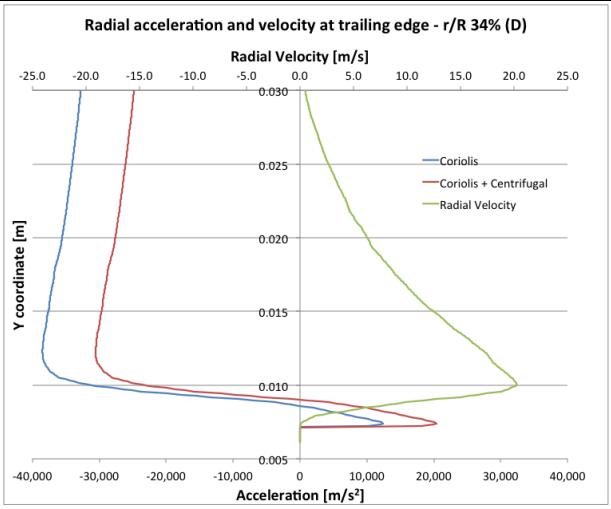

Figure 17: Radial forces and Velocity at r/R 34% for C and D conditions

	Condition **C** – r/R 65%	Condition **D** – r/R 65%
L	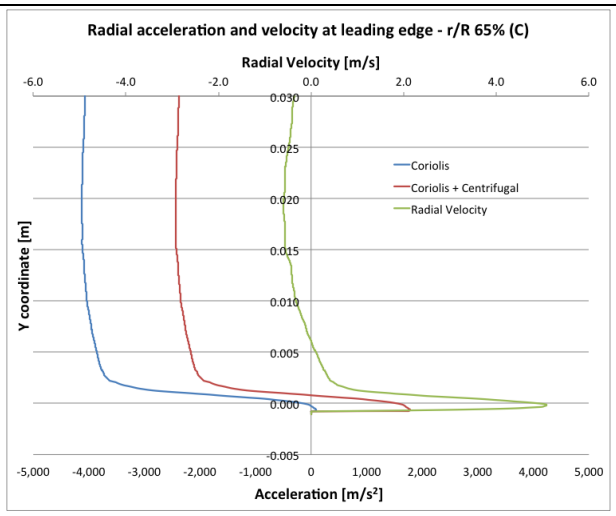	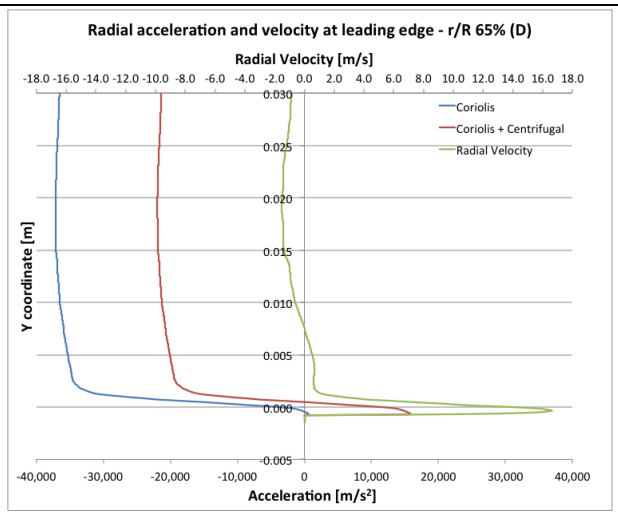
M	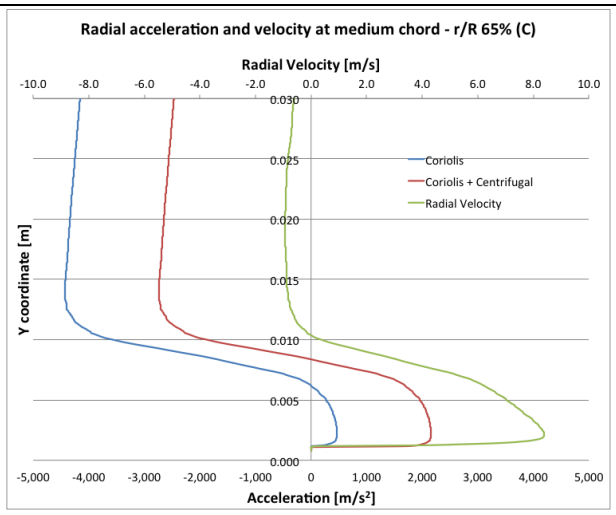	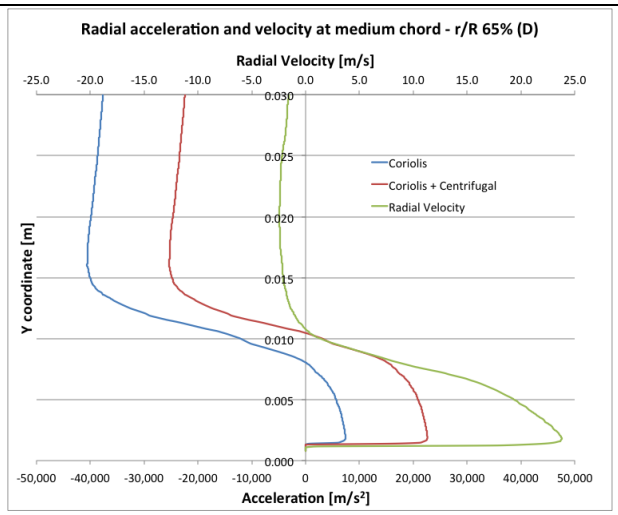
T	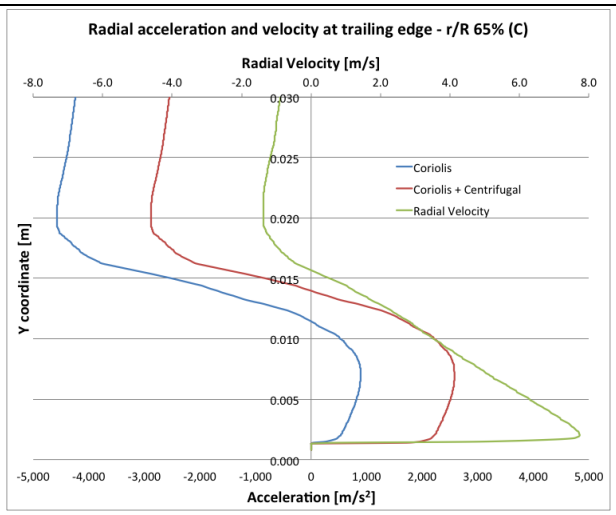	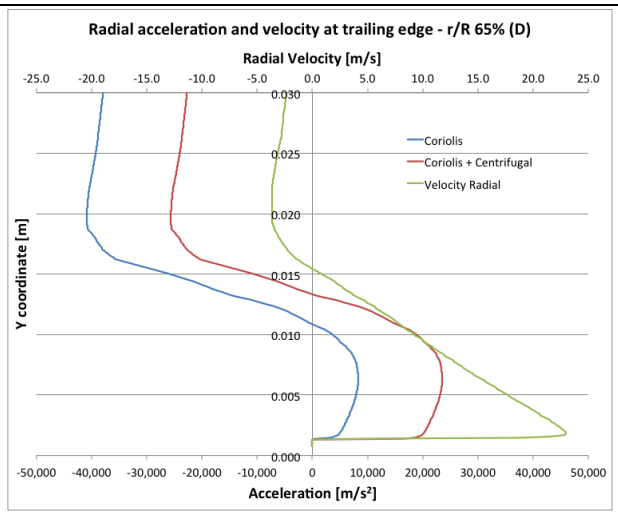

Figure 18: Radial forces and Velocity at r/R 65% for C and D conditions

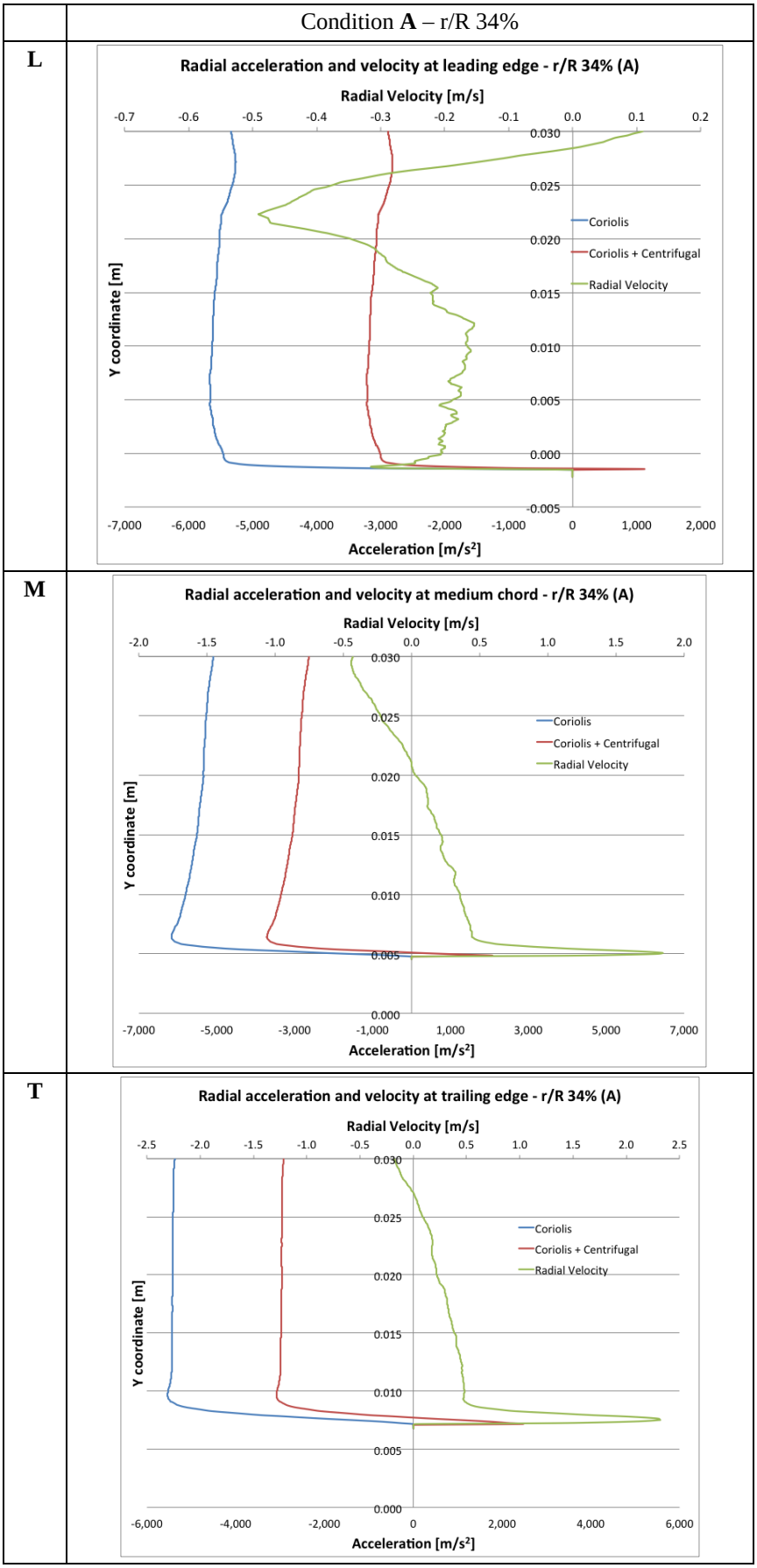

Figure 19: Radial forces and Velocity at r/R 34% for A condition

In Fig. 18, a medium radial station (r/R 65%) is analyzed. The correspondence between radial forces and radial velocity is quite evident. In the lower layers the centrifugal force prevails and the flow is radially accelerated toward the tip. As long as the azimuthal velocity v_θ increases with the distance from the blade, the radial component of the Coriolis forces rapidly increases and the radial velocity is decelerated until it becomes slightly negative, at a certain axial distance. In this case however, the force balance is not sufficient to trigger the onset of the helical vortex as the ratio (12) here in L has a value of only 2.4 for both C and D conditions. Indeed, it is seen in the above that at this radial station no helical structure develops ant the rotational augmentation is almost absent.

In order to complete the analysis, the radial force distribution for the aforementioned attached flow condition A is presented in Fig. 19. Only the data relating to the inner section (r/R 34%) are shown because identical consideration may be made for the other radial sections. It is clear that the radial force effects, in this case, are considerably reduced. In fact, for example, even though the order of magnitude of the radial forces for A and C conditions is comparable, the radial velocity values are much lower in A. Considering also that the rotational velocity in A is 2,500 r/min while in C is 1,500 r/min the lower radial velocity values are ascribable to a reduction of the rotation influence when the flow is mostly attached. This confirms what is found in section 2.1, that in attached flow condition, the rotational forces do not overcome the pressure suction, which maintains the flow like as it is well guided. However, in this specific case, as a slight separation is detected near the trailing edge, the separated layer, subjected to the radial forces, develops in a radial flow at medium chord and trailing edge as evidenced in Fig. 19 (M and T). The correspondence between radial forces and velocity trends is however confirmed.

From a general point of view, the rotational augmentation phenomenon can now be summarized. In Fig. 20 a clear representation of the helical vortex dynamics is shown. Essentially, a fluid element, approaching the leading edge at the inner blade, begins to be subjected to the rotational forces. In the upper separated layer, the high values of the azimuthal velocity component v_θ, lead to high negative radial component of the Coriolis force. The net radial force F_r is thus negative, as evidenced in Fig. 20 by the red vector. For this reason, the flow is definitely deflected toward the hub. As long as the fluid element travels in the streamwise direction, it is decelerated due to the pressure gradient and the strong low pressure at the leading edge.

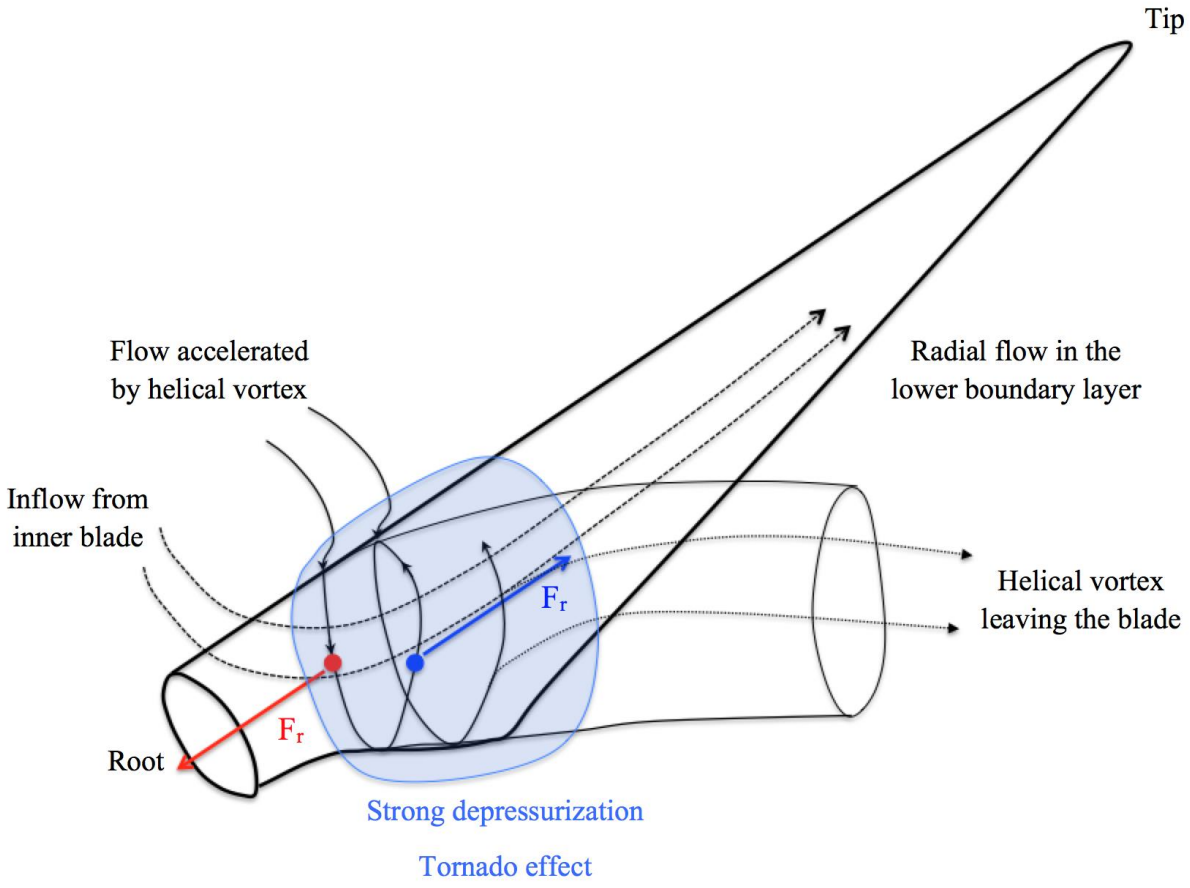

Figure 20: Representation of the helical vortex development dynamics

This reduces v_θ and finally F_{Cor-r}. Indeed, in the lower layer, where v_θ is minor or negative due to the suction and recirculation toward the leading edge, the centrifugal force prevails or is enforced when F_{Cor-r} is positive. Thus F_r becomes positive and is denoted by the blue vector in Fig. 20. The flow is now deflected toward the tip. The tilting of the radial force generates a strong vertical shear, which triggers the vorticity and helicity production in the separated layer and ultimately the onset of the helical vortex. Once the helical vortex develops, the incoming flow is further accelerated and a strong suction is produced. The result is a substantial depressurization with a dynamic similar to that of an atmospheric tornado. In this case, however, the presence of the blade leads to a suction of the entire separated layer almost similar to the flow reattachment shown in Fig. 5.

However, it is quite evident that the main factor, responsible for the rotational augmentation, is the radial component of the Coriolis force that, when the AoA reaches a certain value, acts in equilibrium with the centrifugal force and the pressure gradient, triggering the development of the helical vortex.

Fixed blade results

A further demonstration of the above is obtained by modelling a fixed blade according to what is mentioned in part I of this work. A fixed 3D blade with the same twist and taper of the rotor was simulated by imposing spanwise velocity gradients and radial forces equal to those for condition D. The advantage of simulating the fixed wing, replicating the effects of rotation, is that the hub influence is eliminated, as it can be a source of uncertainty. Moreover, the single rotational effects can be modelled separately, thus highlighting their weight on the augmentation. Indeed, the blade was first simulated by imposing only the spanwise velocity gradient (named as simulation VG). Then the momentum of the radial forces was added (named as simulation MA). According to the cylindrical coordinates of Fig. 16, both the effects of F_{Cor-r} and $F_{Cor-\theta}$ were thus taken into account as well as F_{centr}. It is evident that the flow-field over a fixed wing is different from that on a rotating wing due to the lack of the curved flow but is of great help here for a qualitative analysis. The comparison results are really interesting and are shown in the following figures (Figures 21 – 28).

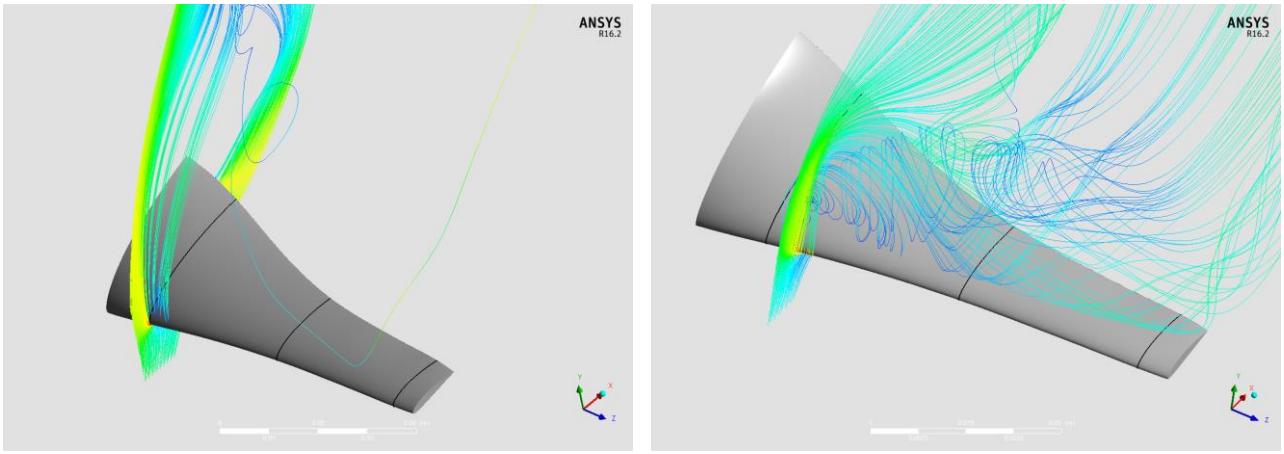

Figure 21: 3D streamline for VG (left) and MA (right) simulations

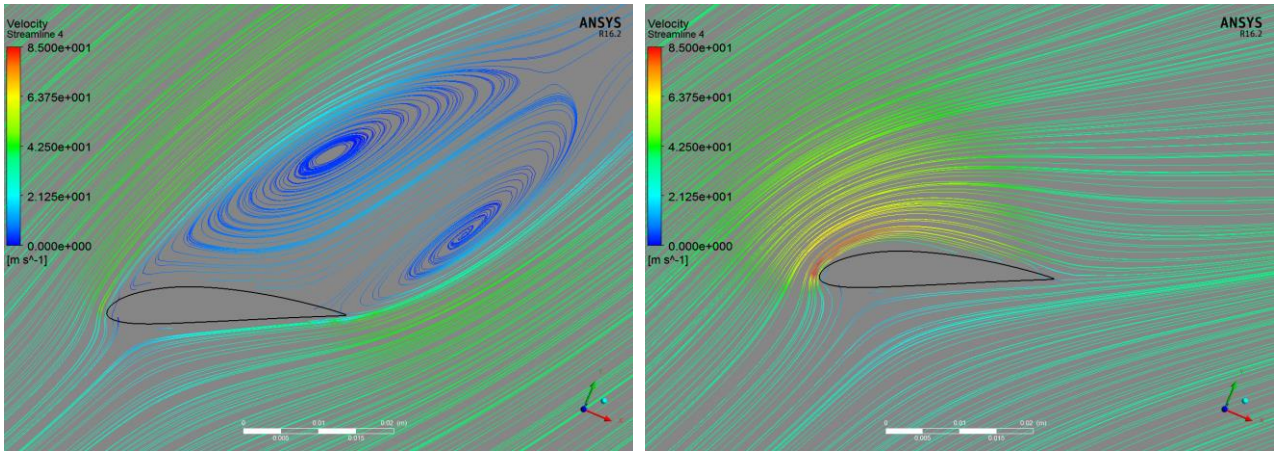

Figure 22: 2D streamlines for VG (left) and MA (right) simulations at r/R 34%

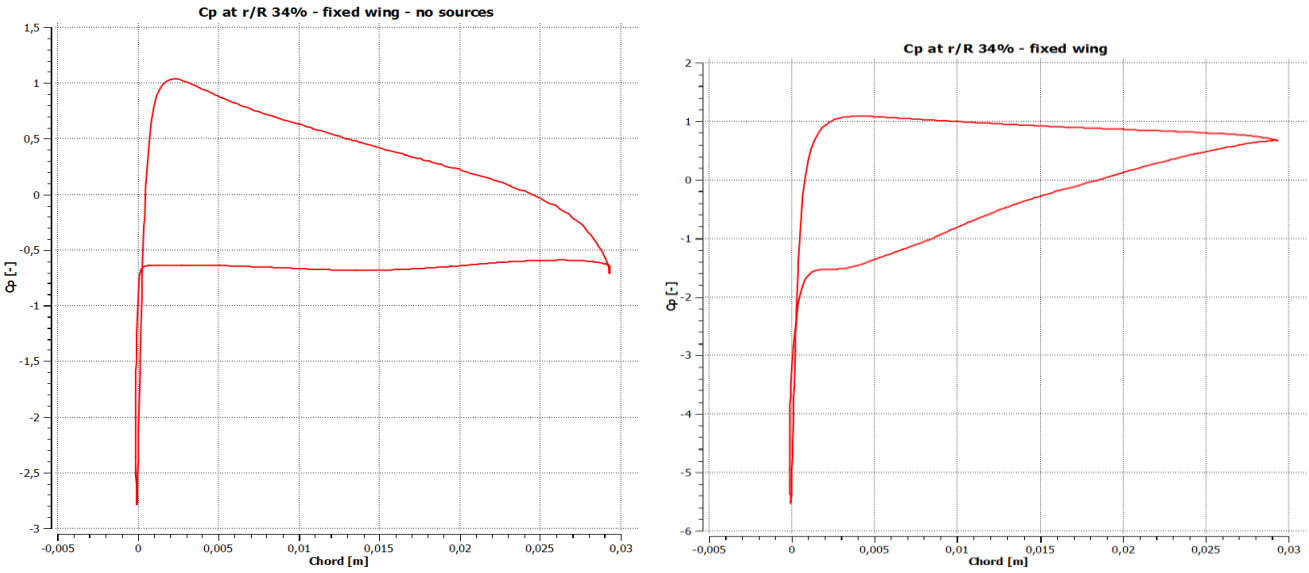

Figure 23: Calculated C_p for VG (left) and MA (right) simulations at r/R 34%

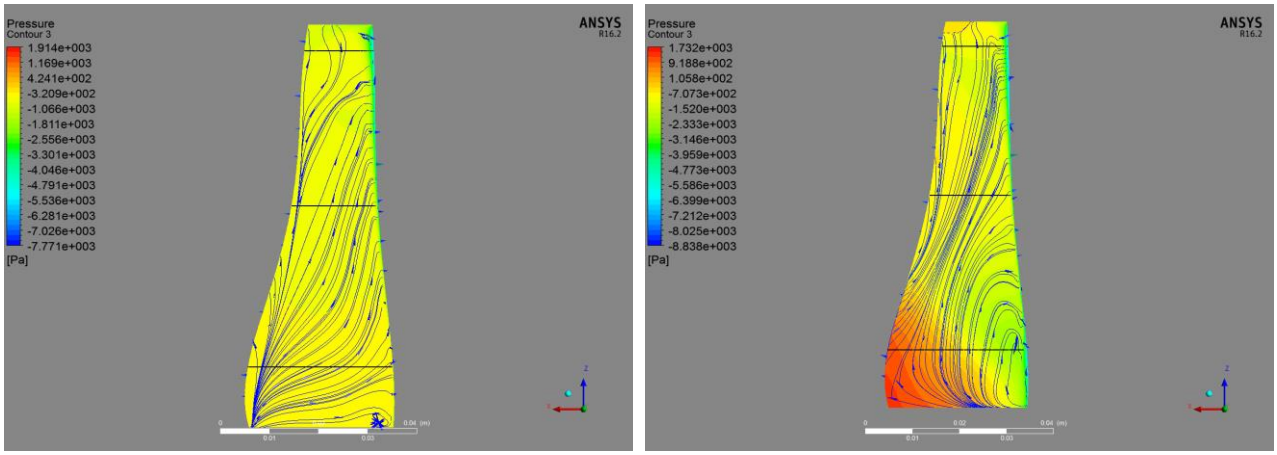

Figure 24: Pressure distribution and wall shear streamlines for VG (left) and MA (right) simulations

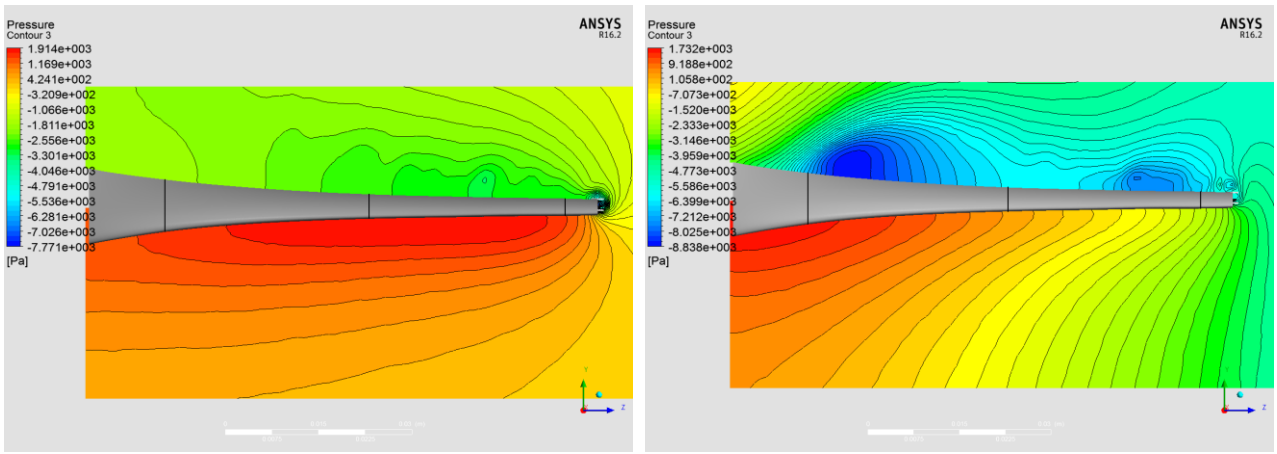

Figure 25: Pressure contours in a section perpendicular to the blade for VG (left) and MA (right) simulations

The hypothesis that the rotational augmentation is strictly related to the helical vortex onset is confirmed in Fig. 23, where the pressure coefficient trends for the fixed wing at r/R 34% are presented. The strong depressurization of the suction side for the MA simulation is almost equal to that in Fig. 5, while the simple velocity gradient generates only a slight depressurization near the leading edge. The flow-field finally comes out nearly reattached, as evidenced in Fig. 22 right.

In Fig. 24, the wall shear streamlines and the pressure contours over the blade show how the rotational forces are capable of modifying both the flow-field and the pressure distribution. In the simulation without momentum sources (Fig. 24 left), the presence of a radial flow is due to the pressure gradient. The pressure decreases in the tip direction and the flow is pushed outward in the lower boundary layer. However the pressure distribution appears regular without a strong depressurization. When the momentum source is present (Fig. 24 right), the flow-field and the pressure distribution drastically change, becoming almost similar to that in Fig. 7. The strong low pressure in the inner blade is evidently related to the onset and development of the helical structure.

From the streamline analysis in Fig. 21 and 22 the strong influence of the radial momentum is evident. While the simple velocity gradient leads to a flow-field similar to that of a 2D condition (Fig. 21 and 22 left), with a fully developed separation, the momentum addition triggers a helical structure in the inner blade, which is noticeably similar to that generated by rotation (Fig. 21 and 22 right). The strong analogy with Fig. 5 and 6 demonstrates the assumption that the radial force balance is mainly responsible for the generation of the coherent helical structures over the blade.

Similar considerations can be made on Fig. 25. Here, the pressure contours are obtained in a section perpendicular to the blade at a mid chord. What is remarkable is the strong similarity between the pressure distribution in Fig. 25 (right) and in Fig. 11. Indeed, even if in the pressure side the contours are different, probably due to the lack of the curved flow, on the suction side both the low pressure areas, at the inner blade and near r/R 80%, are evident. These depressurization areas are clearly related to the development of helical structures, that are absent in VG simulation (Fig. 25 left). This definitely confirms that the radial forces, and specifically the equilibrium between the radial component of the Coriolis force and the centrifugal force over the entire separated layer, generate the shear in such a way that the helical vortices are triggered. The rotational augmentation is thus dependent on the intensity and extension of the helical structures, which in turns depend only on the AoA and on the consequent force imbalance.

In conclusion, in Fig. 26 right, the iso-surfaces of vortex core region show the development of the two helical vortices, quite similar to that in rotating blades (Fig. 13) while the simple velocity gradient leads to a single vortex due to tip effects (Fig. 26 left).

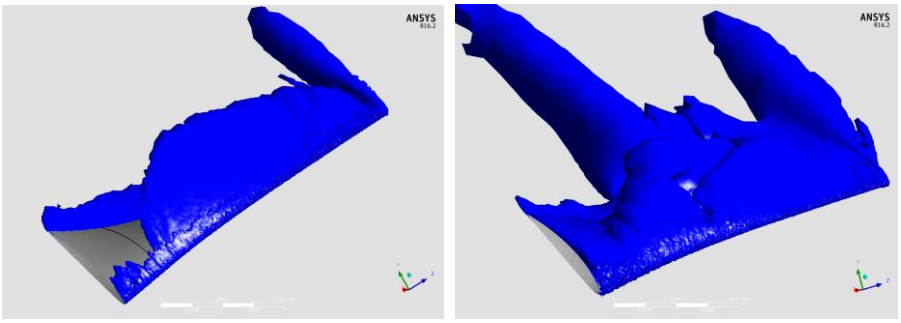

Figure 26: Vortex core region for VG (left) and MA (right) simulations

CONCLUSIONS

The HAWT design and optimization cannot be disregarded from an accurate evaluation of the 3D effects over the blades. While the tip loss models are widely reliable and give accurate results, the centrifugal pumping models are not as accurate and they work well only in limited condition or for specific rotors. The scientific literature recognizes that this is due to the fact that this phenomenon is not yet fully understood. Therefore, an accurate physical comprehension of the rotational augmentation mechanism is an essential key step for a future modelling improvement of this phenomenon.

Based on the scientific literature considerations and by the use of accurate CFD models, the present work provides a new physical explanation of the rotational augmentation, leading the way for a better modelling of this phenomenon inside simplified 1D design codes. Carefully analysing the post processing results of an experimental micro rotor, the authors evaluate a wide range of operative conditions over the entire blade. At lower AoAs, when the flow is attached or the separation is moderate, the rotational effects act by stabilizing

the boundary layer, leading it to a sort of reattachment. In this case, the radial flow, directed from the inner blade toward the tip, flows inside the lower boundary layer thus causing the stall delay. The aerodynamic forces are compatible with the 2D or slightly increased. In this condition, the known stall delay models are probably accurate enough. As the AoA increases, the flow-field becomes increasingly complex. The entire separated layer is subjected to the radial forces. The radial component of the Coriolis force, which is seen to be over four times higher than the other components, causes a flow-deflection toword the hub in the upper separated layer while, in the lower layer the centrifugal force prevails and generates a strong radial flow in the opposite direction. Therefore, the change of the radial force direction causes an axial shear that triggers the onset of a helical vortex in the inner blade. Through the use of pressure contours, streamlines and C_p charts, the coherent helical structure was found to be mainly responsible for the strong depressurization of the suction side of the blade and finally for the noticeable increase of lift and drag coefficients at medium AoAs ($10° < AoA < 60°$ in this case). At higher AoAs the adverse pressure gradient in the streamwise direction is so intense that radial forces are not sufficient to trigger the helical vortex and the flow completely separates. The aerodynamic forces return to being compatible with the 2D one. A radial flow is still present but interests only the lower boundary layer and does not influence the pressure distribution as much. The entire process, from lower to higher AoAs is to be considered gradual as AoAs increase. Therefore, the helical vortex appears at a certain AoA, increases its strength as the AoA increases and finally decreases its effect at higher AoAs. Moreover, the force imbalance is not dependent on wind and rotational speeds, thus the rotational augmentation depends only on AoA.

The accurate analysis of the radial force and velocity, in a maximum augmentation condition, demonstrated the strong correlation between both of these and supports the supposition that the radial component of the Coriolis force is the one that contributes in a decisive way to the development of the rotational augmentation phenomena. This is certainly a new idea as, in the scientific literature, the centrifugal force and the azimuthal component of the Coriolis force are instead considered more important.

The further idea of simulating a fixed wing, separating the spanwise pressure gradient effects from that due to the radial forces, gives important support in the comprehension of the physical mechanism that triggers the rotational augmentation. The development of the coherent helical structure is confirmed as the main cause of the depressurization of the separated layer.

According to the authors' opinions, the above represents an important key step in the physical comprehension of the fluid-dynamics of rotating blades. The application of what has been inferred can be an improvement of the 1D centrifugal pumping models or a rather interesting performance improvements. Indeed, the helical vortex and its effects may be used in order to obtain a desired performance increment in off-design operative conditions. Moreover, the blade structural loads evaluation can certainly be improved, based on a more accurate knowledge of the rotational augmentation.

The analysis of the lift coefficient trends, presented in part I of this work, as well as the streamline behaviour in the maximum augmentation condition, demonstrate a fluid-dynamic behaviour that is quite similar to the inviscid one. This can be an important base in the development of new centrifugal pumping models for the 1D BEM codes.

Certainly, the low operative Reynolds number of the micro rotor used in this paper emphasize the rotational augmentation due to the greater influence of the viscous stress, which is responsible for the momentum transfer between the fluid layers. However, from an accurate study of the NREL PHASE VI HAWT, the authors have found an identical flow-field behaviour, with the development of a coherent helical vortex in the inner blade and a consequent strong depressurization and force augmentation. These results confirm and extend the authors' hypotheses but are not presented here for evident reasons of briefness.

NOMENCLATURE

CFD	Computational Fluid Dynamics
AoA	Angle of Attack
HAWT	Horizontal Axis Wind Turbine
TSR	Tip Speed Ratio
MVR	Maximum Velocity Ratio
MVR_{3D}	Maximum Velocity Ratio for 3D condition
MVR_{2D}	Maximum Velocity Ratio for 2D condition
A, B, C, D, E	Rotor operative conditions
L	Leading edge chord position
M	Medium chord position
T	Trailing edge chord position
VG	Simulation with Velocity Gradient only
MA	Simulation with Momentum Addition
y, θ, r	Cylindrical coordinates
Re	Reynolds Number [-]
n	Rotational speed [r/min]
ω	Angular speed [rad/s]
V_w	Wind Speed [m/s]
V_R	Relative velocity far from the blade [m/s]
V_r	Relative velocity near the blade [m/s]
$V_{s\,max}$	Maximum velocity on the suction side [m/s]
v_y, v_θ, v_r	Velocity components in cylindrical

	coordinates [m/s]
u	Local velocity field [m/s]
C_l	Lift coefficient [-]
C_d	Drag coefficient [-]
C_p	Pressure Coefficient [-]
r	Local radius [m]
R	Rotor radius [m]
dV	Infinitesimal fluid element volume [m^3]
ρ	Air density [kg/m^3]
μ	Dynamic viscosity [Pa s]
p	Pressure [Pa]
ω	Vorticity [s^{-1}]
H	Helicity [m/s^2]
F_y, F_θ, F_r	Force components in cylindrical coordinates [N]
$\mathbf{F_{pg}}$	Force due to pressure gradient per unit mass [m/s^2]
τdS	Force due to viscous shear [N]
F_{centr}	Centrifugal force [N]
$F_{Cor-\theta}$	Azimuthal component of the Coriolis force [N]
F_{Cor-r}	Radial component of the Coriolis Force [N]

REFERENCES

[1] Md. Mahbub Alam, Y. Zhou, H. X. Yang, H. Guo, J. Mi *The ultra-low Reynolds number airfoil wake* Exp. Fluids (2010) 48:81–103 Springer DOI 10.1007/s00348-009-0713-7

[2] S. Wang, Y. Zhou, Md. Mahbub Alam, H. Yang *Turbulent intensity and Reynolds number effects on an airfoil at low Reynolds numbers* Physics of Fluids (1994-present) 26 , 115107 (2014); doi: 10.1063/1.4901969

[3] W. Chen, L. P. Bernal *Design and Performance of Low Reynolds Number Airfoils for Solar-Powered Flight* 46th AIAA Aerospace Sciences Meeting and Exhibit http://dx.doi.org/10.2514/6.2008-316

[4] A. Dovgal, V. V. Kozlov, A. Michalke *Laminar boundary layer separation: Instability and associated phenomena* Progress in Aerospace Sciences 30(1):61-94 · January 1994 DOI: 10.1016/0376-0421(94)90003-5

[5] S. Sunada, A. Sakaguchi, K. Kawachi *Airfoil Section Characteristics at a Low Reynolds Number* Journal of Fluids Engineering 119(1) · March 1997 DOI: 10.1115/1.2819098

[6] P. J. Kuntz *Aerodynamics and Design for ultra-low Reynolds number flight* Ph.D. Thesis Stanford University (2003) Publication Number: AAI3104263; ISBN: 9780496518319

[7] D. F. Kurtulus *On the wake pattern of symmetric airfoils for different incidence angles at Re = 1000* International Journal of Micro Air Vehicles 8(2):109-139 · June 2016 DOI: 10.1177/1756829316653700

[8] Y. Levy, D. Degani, A. Seginer *Graphical Visualization of Vortical Flowsby Means of Helicity* AIAA Journal VOL. 28, NO. 8, August 1990 pp. 1347 – 1352 DOI: 10.2514/3.25224

[9] H. K. Moffatt, A. Tsinober *Helicity in laminar and turbulent flow* Annu. Rev. Fluid Mech. 1992. 24(1) : 281-312 DOI: 10.1146/annurev.fl.24.010192.001433

[10] H. K. Moffatt *Helicity and singular structures in fluid dynamics* Proc. Natl. Acad. Sci. USA 2014 Vol. 111, no. 10 doi: 10.1073/pnas.1400277111

[11] J. C. R. Hunt, F. Hussain *A note on velocity, vorticity and helicity of inviscid fluid elements* J. Fluid Mech. (1991), vol. 229, pp. 569-587 DOI: https://doi.org/10.1017/S0022112091003178

[12] M. Jiang, R. Machiraju, D. Thompson *Detection and Visualization of Vortices* DOI: 10.1016/B978-012387582-2/50016-2

[13] D. F. Scofield and P. Huq *Evolution of helicity in fluid flows* J. Math. Phys. 51, 033520 (2010); doi:10.1063/1.3329422

[14] G. P. Corten *Flow Separation on Wind Turbine Blades* Utrecht University ISBN 90-393-2582-0,NUGI 837 https://dspace.library.uu.nl/bitstream/handle/1874/653/full.pdf